Iraqi National Journal of Earth Science

www.earth.mosuljournals.com

Seismic, Petrophysics, and Attribute Analysis to Evaluate the Tertiary Reservoir in the High Folded Zone, Kurdistan Region-Iraq

Kakarash I. Gardi[1'*], Bakhtiar Q. Aziz [2], Ezzadin N. Baban [3]

[1'] Department of Geology, College of Science, University of Sulaimani, Sulaimani, Iraq.*
General Directorate of Dam and Reservoirs, Kurdistan Region, Erbil, Iraq.
[2] Department of Geology, College of Science, University of Sulaimani, Sulaimani, Iraq.
[3] Department of Geology, College of Science, University of Sulaimani, Sulaimani, Iraq.

Article information

Received: 31- Jul -2023

Revised: 21- Nov -2023

Accepted: 20- Dec -2023

Available online: 01- Jul– 2024

Keywords:
Seismic interpretation
Reservoir characterization
Attribute analysis
Petrophysical analysis
3D static modelling

Correspondence:
Name: Kakarash I. Gardi

Email:kakarashgeo@gmail.com

ABSTRACT

The present study is intended to evaluate one of the oil-bearing horizons in the (WN) oil field within the High Folded zone in the Kurdistan Region of Iraq, which represents a carbonate reservoir of the Tertiary units. Also, the picking and mapping of two other horizons of interest from the top and bottom of the reservoir horizon are done across the area. This work is achieved using 3D seismic data, check shots, and well logs. The methodology involves several processes including data loading, well seismic tying, horizon and fault identification and interpretation, velocity modelling, time-depth conversions, petrophysical analysis, and 3D properties modelling. Isochron and depth maps for three horizons and two isopach maps are constructed. An asymmetrical doubly plunging rollover anticlinal closure with a length of 6.4 km and width of 3.5 km is identified on the reservoir maps that trend in the East-West direction. Faults are identified and extracted manually and automatically. A total eighteen of minor reversal faults striking the northern flank of the anticlinal closure are interpreted. Variance, Chaos, and Ant Tracking attributes are selected and applied successfully that help to better visualize fractures and automatic fault extraction. Petrophysical analysis and cross-plots demonstrates that the reservoir consists of dolomite, lime dolomite, and anhydrite limey dolomite. The petrophysical properties reveal the average of each effective porosity, secondary porosity, permeability, clay volume, and water saturation of the reservoir at 9.98%., 4.39%., 14.1 milli Darcy, 9.13%, and 47.8% respectively. The study shows that the reservoir has moderate hydrocarbon prospects.

DOI: 10.33899/earth.2023.142239.1121,

التحليل الزلزالي والبتروفيزيائي والسمات لتقييم الخزان الحقب الثلاثي في نطاق الطيات العالية، إقليم كوردستان، العراق

كاكه ره ش ابراهيم طة ردي[1] ، به ختيار قادر عزيز[2] ، عزالدين نجم الدين بابان[3]

[1] قسم علوم الأرض، كلية العلوم، جامعة السليمانية، السليمانية، العراق

المديرية العامة للسدود والخزانات المائية، إقليم كوردستان، أربيل، العراق

[2] قسم علوم الأرض، كلية العلوم، جامعة السليمانية، السليمانية، العراق

[3] قسم علوم الأرض، كلية العلوم، جامعة السليمانية، السليمانية، العراق

معلومات الارشفة

تاريخ الاستلام: 31- يوليو -2023

تاريخ المراجعة: 21- نوفنبر -2023

تاريخ القبول: 20- ديسمبر -2023

تاريخ النشر الالكتروني: 01- يوليو-2024

الكلمات المفتاحية

التفسير الزلزالي

توصيف الخزان

تحليل السمات

التحليل البتروفيزيائي

النمذجة الثابتة ثلاثية الأبعاد

المراسلة:

الاسم: كاكه ره ش ابراهيم طة ردي

Email: kakarashgeo@gmail.com

الملخص

تهدف الدراسة الحالية إلى تقييم أحدى الآفاق الحاملة للنفط في حقل " WN " داخل نطاق الطيات العالية في إقليم كوردستان العراق، والذي يمثل مكمنا من الصخور الجيرية ضمن وحدات الحقب الثلاثي. ، تم أيضًا التقاط ورسم خرائط لأفقين آخرين مهمين من أعلى وأسفل أفق الخزان عبر المنطقة. تم إنجاز هذا العمل باستخدام البيانات الزلزالية ثلاثية الأبعاد، ضربات التدقيق، وسجلات الآبار. شملت المنهجية عدة عمليات بما في ذلك تحميل البيانات، ربط البئر بمقطع الزلزالي، تحديد وتفسير الأفاق والفوالق، نمذجة السرعة، تحويلات العمق-الزمن، التحليل البتروفيزيائي، ونمذجة الخصائص ثلاثية الأبعاد. تم إنشاء خرائط الزمن والعمق للآفاق الثلاثة وخريطتين من خرائط السمك. بينت خرائط الخزان وجود طية محدبة غير متناظرة وثنائية الغطس بطول 6.4 كم وعرض 3.5 كم والتي تتجه باتجاه شرق-غرب. حددت الفوالق واستخرجت يدوياً وتلقائياً. تم تفسير ثمانية عشر فالقاً من الفوالق المعكوسة الصغيرة التي ضربت الجناح الشمالي للطية المحدبة. تم اختيار سمات (ملامح) التباين والفوضى وتتبع النمل وطبقت بنجاح مما ساعدت على تبيان الكسور بشكل أفضل واستخراج الفوالق بشكل تلقائي. أظهر التحليل البتروفيزيائي بأن المكمن يتكون من الدولوميت والدولوميت الجيري والدولوميت الجيري الأنهيدرايتي. أظهرت الخصائص البتروفيزيائية أن المعدل لكل من المسامية الفعالة والمسامية الثانوية والنفاذية وحجم الطين والتشبع المائي للمكمن بنسبة .9.98%، 4.39%. ، 14.1 ملي دارسي، .9.13% ، 47.8% على التوالي. وأظهرت الدراسة أن المكمن يتمتع بآفاق هيدروكربونية متوسطة.

DOI:10.33899/earth.2023.142239.1121,

Introduction

The study area is located within the administrative boundaries of the Duhok province, which lies to the northwest of Duhok City in the Kurdistan Region of Iraq (KRI) (Fig. 1.a & b). The traditional 2D surveys with linear spread have limitations merely providing several sparsely seismic cross-sections of the subsurface, whereas 3D surveys with a real spread provide a complete picture of the subsurface (Alsadi, 2017). 3D seismic reflection techniques

have become popular in hydrocarbon exploration, which offers the most precise, continuous volumetric seismic coverage to map and delineate subsurface geology (Hart, 1999). The reservoir is fully covered by a 3D seismic survey that makes it possible to fill in the spatial gap between the wells (Varela et al., 2006). A combination of various data sets is necessary for 3D reservoir characterization to infer and identify subsurface geology in more detail (Johann et al., 2001). Integration of a 3D seismic data set with well-log data is incredibly helpful in evaluating the reservoir because it can demonstrate the vertical and lateral distribution of specific reservoir properties (Arifin, 2016). For reservoir characterization, numerous studies have been implemented worldwide using the integration of seismic data and well log data (e.g. Ashraf et al., 2019; Osinowo et al., 2018) and in Iraq (Khawaja and Thabit, 2021) among others. The Zagros thrust-fold belt is a rich hydrocarbon province. More than 5% of the global hydrocarbon reserves are located in this belt (Reif et al., 2012). The Kurdistan region-Iraq forms part of this belt. Although over nearly two decades, 3D seismic exploration in the region has been started, yet not been fully explored and no research has been published. This research focused on using a 3D seismic cube and well-log data to evaluate one of the Tertiary carbonate reservoirs in the High Folded Zone of the structural division of Iraq (Fig. 1.a). In this study, besides tracking the targeted oil-bearing horizon, it is also preferred to pick and map two other interesting horizons, and then using them to build 3D static modelling for the reservoir. According to Aqrawi et al. (2010), Horizon-1 (H1) of Middle Miocene forms a regional cap rock, Horizon-2 (H2) of Middle Miocene forms a hydrocarbon reservoir, and Horizon-3 (H3) of Early Miocene can be a hydrocarbon reservoir and/or local seal rock. Horizon-2 is widely distributed throughout Iraq and is significant as it forms the oil reservoir. The Mesozoic source rocks are the most likely sources for this reservoir.

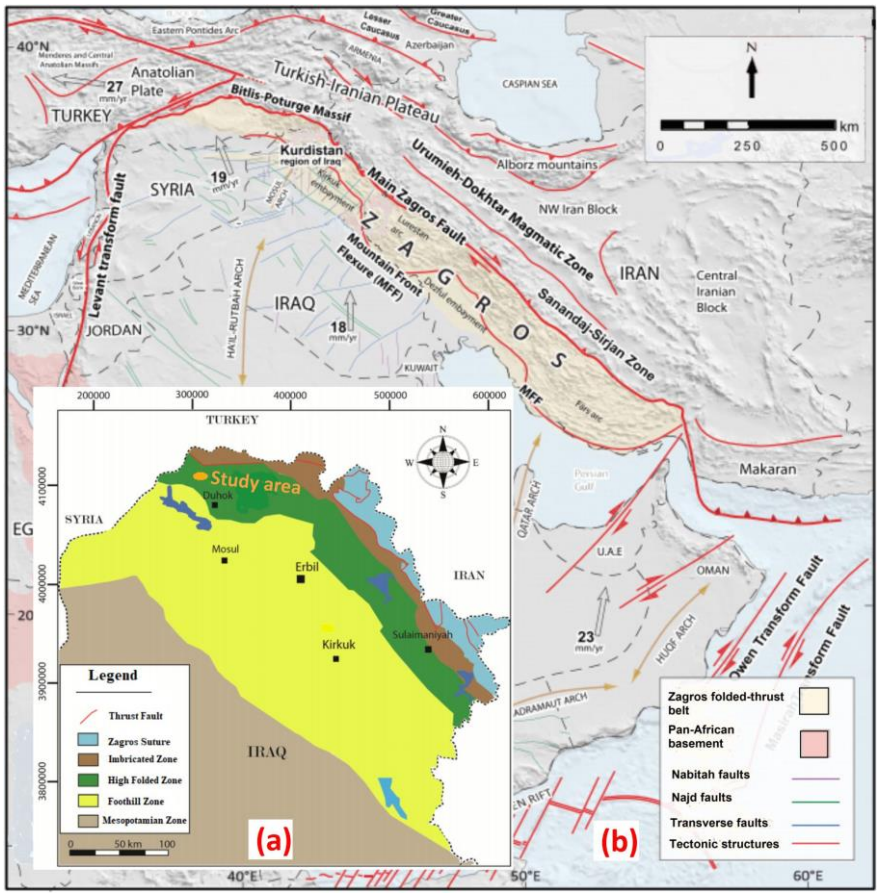

Fig.1. (a) Tectonic map of Iraq showing the study area (from Edilbi et al., 2019), and (b) Tectonic map of the Zagros Fold-Thrust Belt showing the main tectonic elements (modified from Koshnaw et al., 2020).

Due to the complicated and heterogeneous structure, characterizing and modelling carbonate reservoirs is a challenging task (Bueno et al., 2014). Despite this challenge, 3D static modelling represents an effective technique in characterizing reservoirs, thus this study is conducted to create a 3D geological model of this carbonate reservoir to evaluate and shed light on it utilizing all available 3D seismic data, check shots, and well-log data.

The study area lies in the High Folded Zone, which represents a rugged topography mountainous area characterized by high anticlines and narrow synclines. Due to tectonic movements and uplifting, Cenozoic successions widely cropped out and covered the entire area and surroundings (Fig. 2). In some parts, Quaternary and Holocene surface deposits overlie the outcropped formations. A summary of exposed rock formations according to (Van Bellen et al., 1959) is given in Table (1).

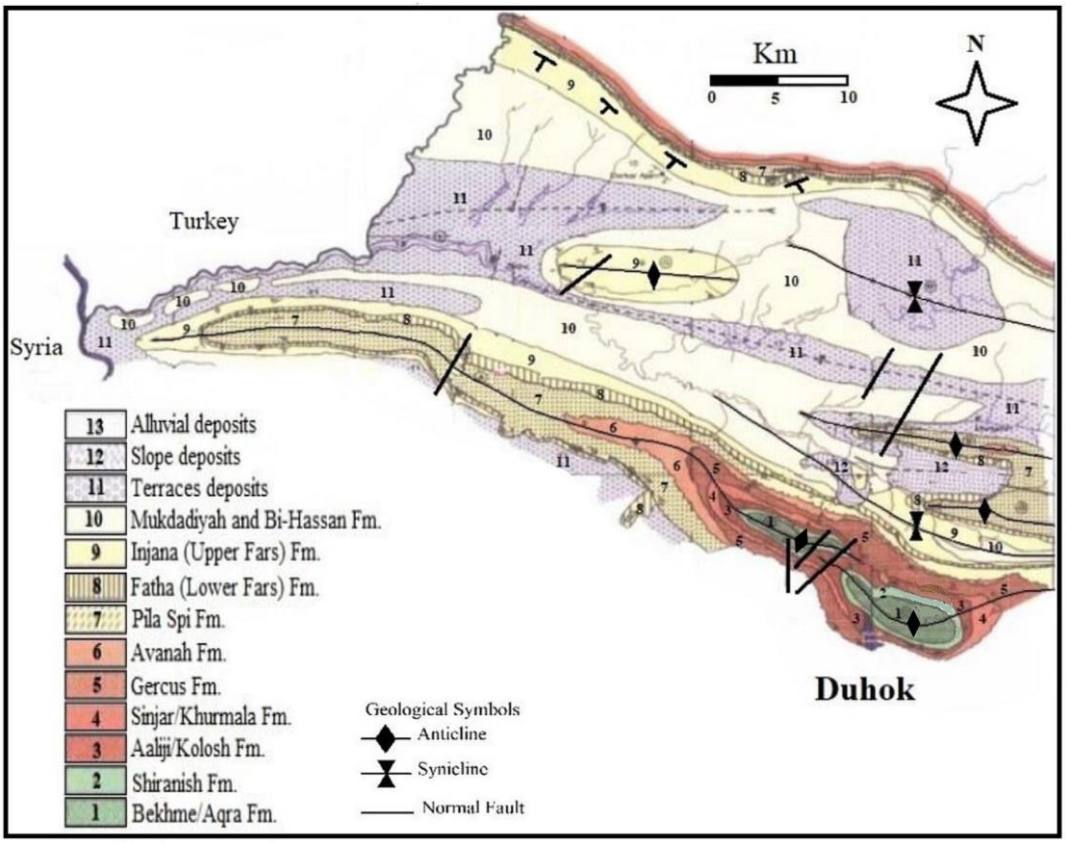

Fig.2. Surface geological map of the study area and its surrounds (from Bamerni et al., 2021).

The High Folded Zone is situated on the northern margin of the Arabian Plate (Fig. 1.b) and forms a part of extensive the Zagros-Taurus Fold and Thrust Belt which extends for almost 2000 km and 200-300 km wide from the Strait of Hormuz in the southern part of Iran NW-ward through the Kurdistan Region to the eastern part of Turkey within the Alpine–Himalayan orogeny (Zainy et al., 2017).The belt and its associated foreland basin resulted from the closure of the Neo-Tethys Ocean, and the subsequent plate convergence and collision of the Arabian plate with the continental Eurasian plate (Iranian and Turkish), which started from the late Cretaceous and continues to the present-day (English et al., 2015). The structural features of the belt in the KRI mostly have two major trends, an NW-SE trend paralleling the Zagros Mountains and an E-W trend paralleling the Taurus Mountains of southern Turkey (Jassim and Goff, 2006). In the KRI, the Zagros-Taurus foreland basin was filled with a thick sedimentary succession that varies from 7 km to 14 km (Al-Azzawi, 2013),

and in particular, within the Duhok area ranges between 8 km to 11 Km (Doski and McClay, 2022).

Table 1. A brief description of the outcropped formations in the area.

Formation	Age	Description
Upper Bakhtiari (Bai Hassan)	U. Pliocene	Conglomerate, siltstone, claystone, and sandstone
Lower Bakhtiari (Muqdadiya)	L. Pliocene	Sandstone, mudstone, and siltstone
Upper Fars (Injana)	U. Miocene	Thin bedded sandstone and claystone
Lower Fars (Fatha)	M. Miocene	Anhydrite, gypsum, marl, and limestone
Pila Spi	M.-U. Eocene	Bituminous dolomitic and chalky limestone
Avanah Limestone	M.-U. Eocene	Limestone is usually dolomitized and recrystallized
Gercus	M. Eocene	Mudstones, sandstone, and sandy and gritty marl

Materials and Methodology

1- The 3D seismic cube consisting of 536 inlines (from 3500 to 4035) and 491 crosslines (from 2150 to 2640) covers a semi-rectangular area of some 37 square km, and suites of composite logs from four boreholes with their check shot data are used to evaluate one of the Tertiary reservoirs of interest. Figure (3) is a seismic base map of the study area showing inlines and crosslines coverage of the 3D seismic survey and well locations. The length of each inline equals 5.880 km with 12 m intervals and the length of each crossline equals 6.420 km with 12m intervals. Data are kindly provided by the International Oil Companies operating in the region through the Ministry of Natural Resources of the Kurdistan Regional Government. Schlumberger's Petrel Suite seismic interpretation software 2017.4 and Senergy's Interactive Petrophysics (IP) software version v4.5.5 windows- based are used for the geophysical and geological evaluation of the study area.

2- Initially, the original 3D seismic data cube are in SEG-Y format of the study area, and the check shots, well tops, and well logs of the four wells within the area are separately imported into a Petrel. Then, the 3D seismic data are realized (converted) into the ZGY bricked format which is regarded as a compressed physical copy that helps to handle and manipulate large databases much quicker than the traditional SEG-Y format (Schlumberger, 2010). Afterwards, using a frequency filter to suppress unwanted noise and increasing the signal/noise ratio (Osaki, 2015) by selecting the Ormsby filter type and Hamming taper because they demonstrated the greatest noise reduction with the least amount of seismic energy loss (Grabeel, 2018). Next, automatic gain control (AGC) to regulate and equalize the root mean square (RMS) amplitude decay with time over a given window is used.

3- The Synthetic seismogram is created at the WN.1 well using calibrated sonic and density logs for computing the acoustic and reflection coefficients with a check shot from the same well. First, the interpretation of horizons on the vertical seismic sections at the well-tie point was started and proceeds outward from there. All seismic sections are checked for the presence of major faults. While eighteen of the visible subtle faults are detected and marked on the horizons, the existence of such faults is not found.

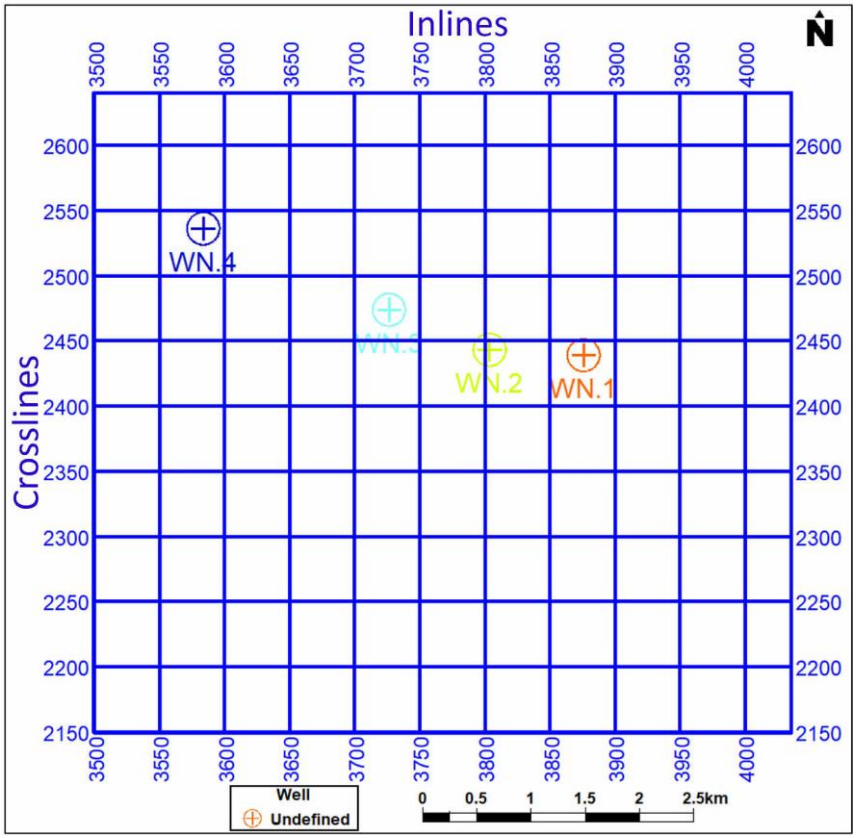

Fig.3. Base map of the study area displaying the 3D seismic coverage and well locations.

4- Manually, horizon picking is performed on every fifth inline and crossline, then filled in between by auto-tracking method. In addition, inserting an arbitrary intersection line or a time slice in the situation where there is ambiguity regarding the continuity of the horizon in question. Although, it is not necessary to track horizons on every inline and crossline, due to the fractured zone in the northern part of the area and there is no properly working auto-tracking technique in this zone, for precise mapping of the horizons further adjusting to a denser grid is taken. Once, the picking of the horizons across the area is completed, the data are directly converted to surfaces to acquire the time structure maps, and eventually, an isochron map for each of them is constructed.

5- Converting the isochron maps to depth maps requires to construct a velocity model. Six equations in Petrel 2017 can be used to create an advanced velocity model. The Eq. (1) for the construction velocity model is selected, which incorporates the V_0, K, and Z values and uses the relationship of linear variation of velocity with depth. This model has been applied by Ten Veen et al. (2019) and other researchers. This model has been applied by Al-Ridha et al. (2018), Toba et al. (2018), and Ten Veen et al. (2019).

$$V=V_0+K*Z \quad \text{……. (Eq. 1) (Schlumberger, 2010)}$$

Where; V is a velocity at any depth of the reflector, V_0 is an initial instantaneous velocity in ms^{-1} at the top of the reflector from the seismic reference datum, constant K is a vertical velocity gradient (compaction factor) in s^{-1}, and Z is actual reflector depth (Ogbamikhumi and Aderibigbe, 2019).

The velocity V_0 and velocity gradient K for each horizon are individually calculated using check shots from all the wells WN.1, WN.2, WN.3, and WN.4. The velocity of horizons H1, H2, and H3 are calculated and they equal to (2057 m/s, 1744 m/s, and 2253 m/s) respectively; and K values equal (0.88 s^{-1}, 1.3 s^{-1}, and 0.65 s^{-1}) respectively. The constructed velocity model by implementing the moving average interpolation method is

used to convert the isochrone maps of all horizons to the depth maps. Two isopach maps have been constructed between H1& H2 and H2 & H3 to show the variable thickness of the cap rock formation (Fig. 10.a) and the thickness of the targeted reservoir formation throughout the area (Fig. 10.b).

6- A structural framework of the static model is defined and created in the depth domain which resembles a skeleton that allows for incorporating both structural and property models in the unified model. After the manipulation and editing, eighteen of the picked subtle faults on seismic sections across the area are used for building the structure framework. A boundary of the target study area is determined and inserted into the model. Then, using the horizon modelling process, all three depth maps of the horizons are combined into the framework. To generate a 3D grid, the structural framework is converted to a fault model, and a structural skeleton is produced through the pillar gridding process. Each corner of the resulting grid cell will have one pillar, which is set in between the faults. Once faults are modelled and adjusted, pillar editing, and all other necessary processing is done. Then, for zonation, two thickness isochore maps are constructed and used as inputs for zone modelling by which two zones between the already modelled horizons were produced. The next step, for increasing assurances of petrophysical modelling by layering (sub-dividing the grid) process, the first zone and second zone are divided into sixty and fifty layers respectively.

7- Preconditioning the seismic data is necessary to improve their quality before any interpretation, especially when applying Ant Tracking attributes. Frequency filter and AGC filtering and then structural soothing for further improvement were applied to the realized seismic data cube. However, while manually interpreting and determining faults is a time-consuming task, tedious, and lacks accuracy (Pedersen et al., 2002), eighteen different minor faults are identified, marked, and labelled F1 to F18 on the interpreted seismic sections to define the appropriate positions of their surfaces and then used in the 3D static model construction. Besides manual picking, the fascinating fault detection and automatic extraction technique-based Ant Tracking algorithm can be implemented to extract fault surfaces from the seismic data in a 3D volumetric attribute (Pedersen et al., 2002) based on Variance (Donahoe and Gao, 2016), Chaos (Aliouane and Ouadfeul, 2014) and both attributes (Kozak, 2018) and several others. The Variance and Chaos (Jiratitipat, 2020) are the two most often attributes utilized to enhance fault and discontinuity in seismic data. To isolate the area of interest, the cube is cropped into a sub-volume. Afterwards, the Variance and Chaos attributes are applied to the cropped cube. In the next step, they are used as inputs to precondition the seismic cube for applying the Ant Tracking attribute.

8- The available log data for analysis and estimation of the petrophysical properties from wells WN.2 and WN.3 are imported to the interactive petrophysics software IP. Suites of composite logs from wells WN.2 and WN.3 including gamma-ray (GR), calliper, bit size (BS), resistivity, bulk density, and neutron porosity logs. As the well-log reports are not available for this work, therefore any corrections for the environmental conditions are not implemented. In addition, the formation temperatures which are necessary for estimating properties also unavailable. Therefore, an average temperature gradient in the Kurdistan Region of 21°C /km (Abdula, 2017) with a reference surface temperature of 25°C is used to estimate the essential petrophysical parameters such as total, effective, and secondary porosity, permeability, clay (shale) volume, and water saturation (Sw). These analyzed properties are loaded into the Petrel software for building a 3D static geological model. Effective porosity, secondary porosity, water saturation, and clay volume are calculated by applying and selecting an appropriate equation provided by the IP software. For porosity determination, the volume of clay is taken into account. A computer-processed

interpretation of well logs is performed for wells WN.2 and WN.3. by a combination of the Gamma Ray Neutron-Density cross-plot method and M-N lithology cross-plots which allowed for determining porosity and lithology.

9- Upscaling well logs can be done in various ways including arithmetic, geometric, and harmonic methods. The arithmetic averaging method has been used for upscaling porosities, clay volume (VCL), and water saturation (Sw), while the harmonic averaging method for permeability has been used. The petrophysical model which is a geostatistical-based algorithm includes a process for determining petrophysical log properties and their distribution throughout the reservoir. The sequential Gaussian simulation (SGS) algorithm, which is one of the popular techniques (Ortiz, 2020) has been used to produce this model. Five upscaled petrophysical properties such as effective porosity, secondary porosity, permeability, water saturation (Sw), and clay volume (VCL) have been incorporated into the previously constructed 3D structural framework to visualize their spatial distribution within the 3D grid. The Buckles plot is constructed just for Horizon-2 at wells WN.2 and WN.3.

Results

Seismic-well data tying are roughly perfect at the well locations, so any stretch and squeeze of the synthetic seismogram to force matching or adjusting are not performed (Fig. 4.a). The targeted horizon-2 (H2) and two other interesting horizon-1 (H1) and horizon-3 (H3) are identified and marked on the seismic section with high certainty (Fig. 4. b).

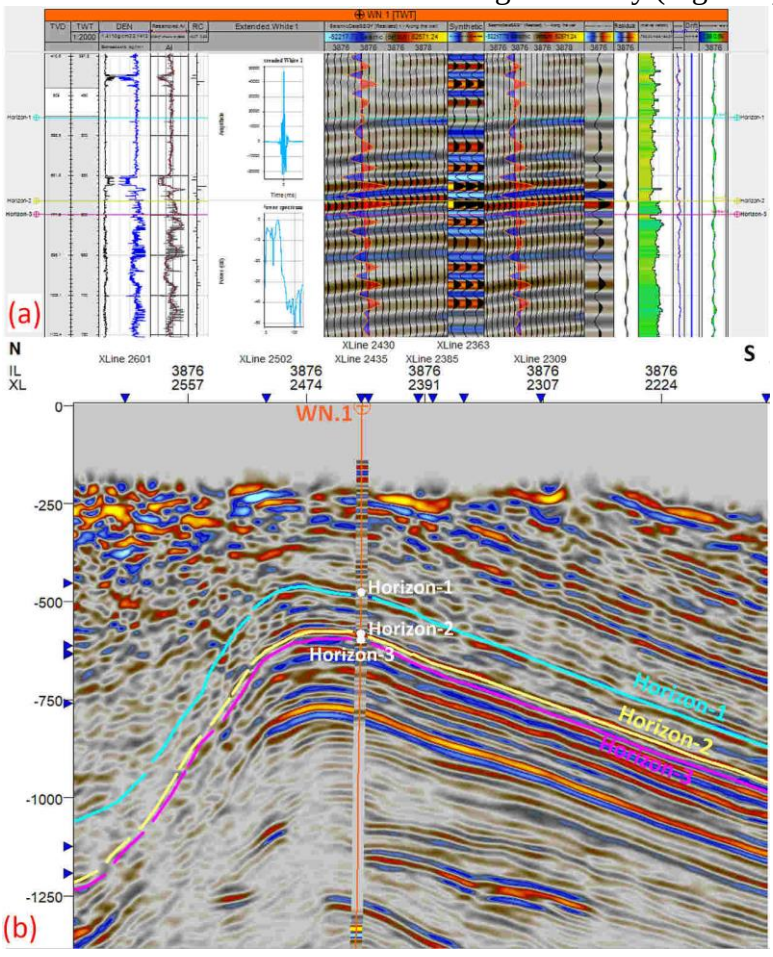

Fig.4. (a) The synthetic seismogram generated from the well WN.1 showing a good match with the seismic section, and (b) The synthetic seismogram and the picked horizons on the seismic section of the Inline No. 3876.

The isochron maps have been constructed for the horizons as displayed in (Fig.5.a), (Fig.6.a), and (Fig.7.a). The two-way-time (TWT) values of the top of the H1, H2, and H3 range from (467.50 to 1135.15), (570.54 to 1272.45), and (581.57 to 1292.33) milliseconds (ms) respectively. The depth maps of the top of the H1, H2, and H3 have been generated as shown in (Fig.5.b), (Fig.6.b), and (Fig.7.b), their depth range from (558.98 to 1309.75), (732.10 to 1529.58), and (774.35 to 1554.71) m respectively.

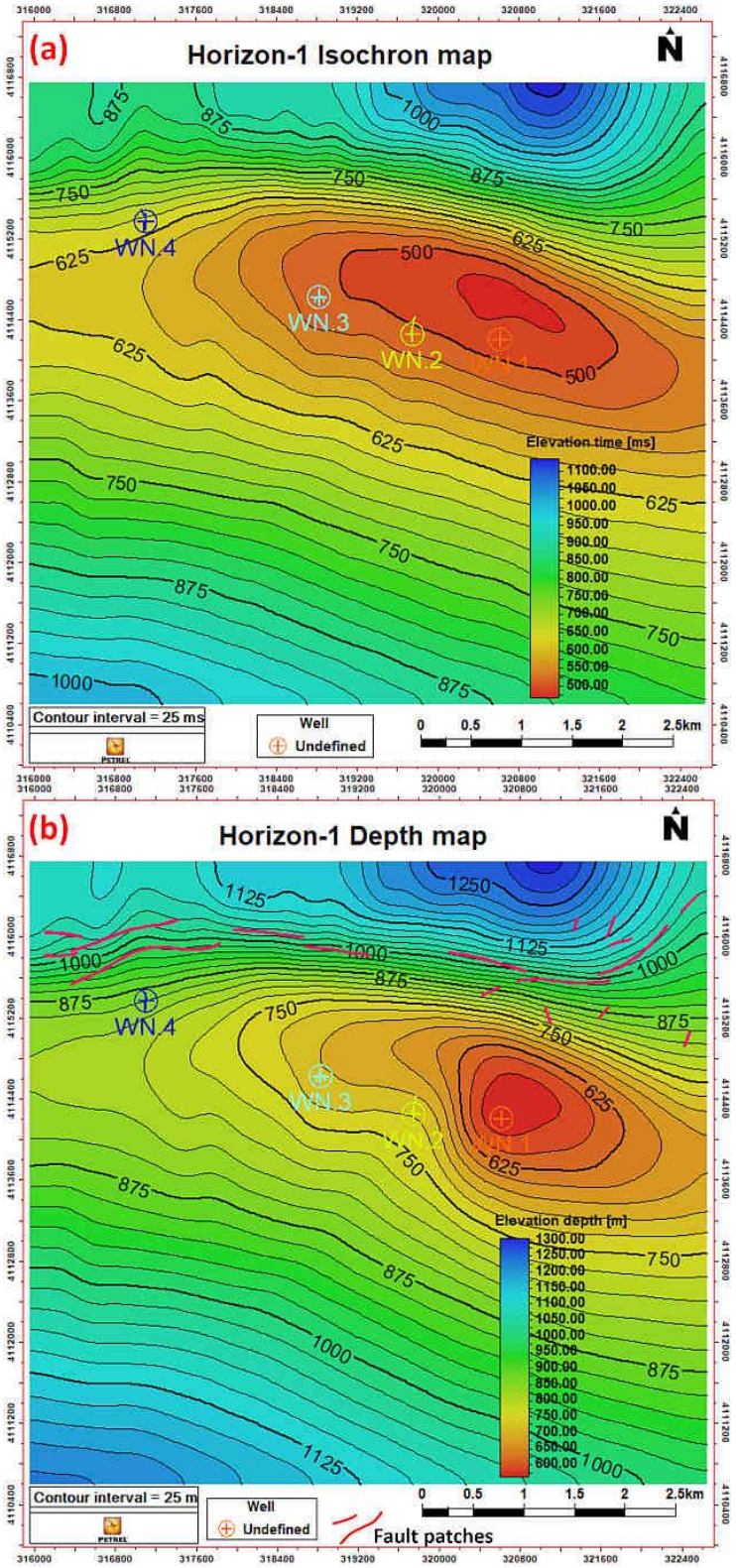

Fig.5. (a) The isochron of the Horizon-1, and (b) The depth map of the Horizon-1.

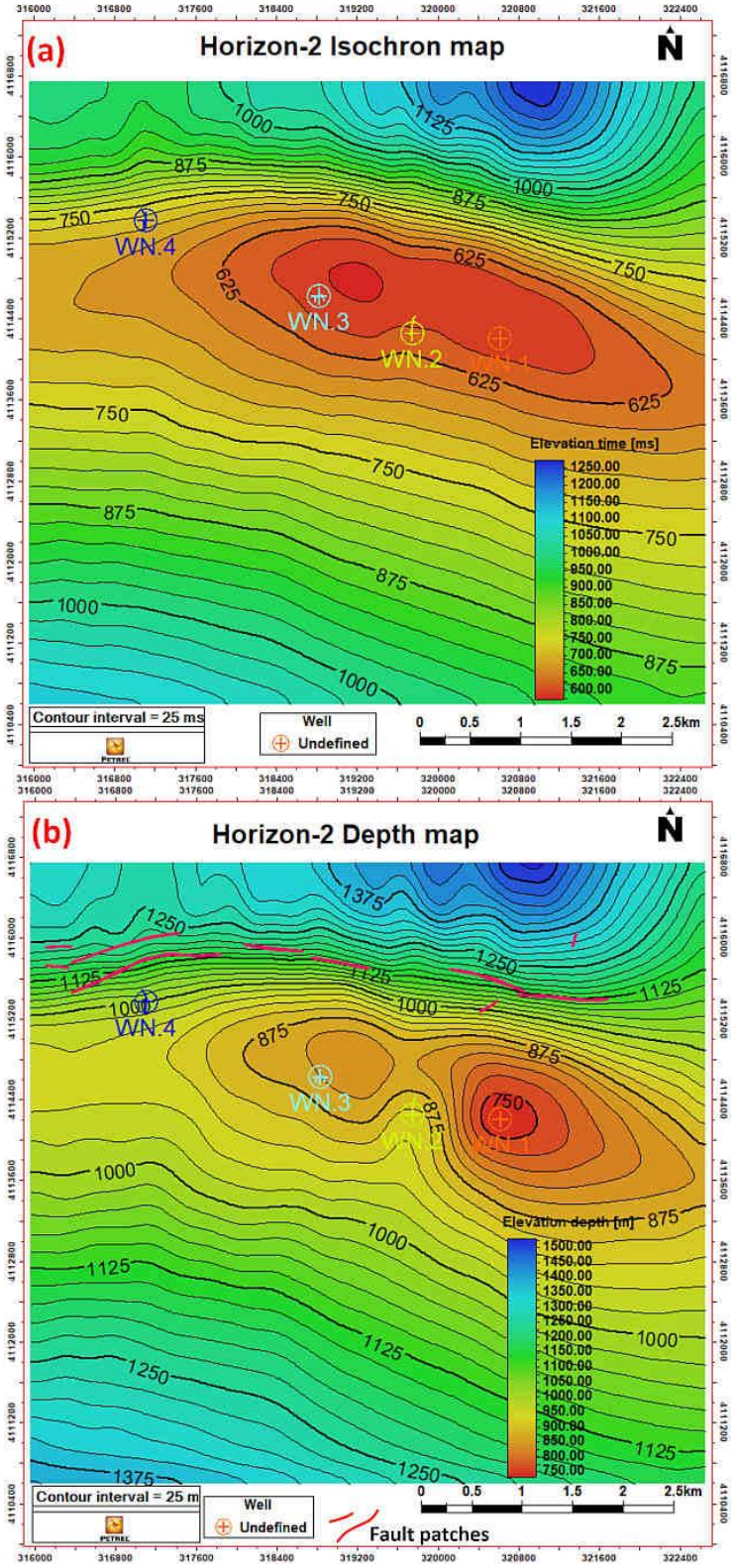

Fig.6. (a) The isochron of the Horizon-2, and (b) The depth map of the Horizon-2.

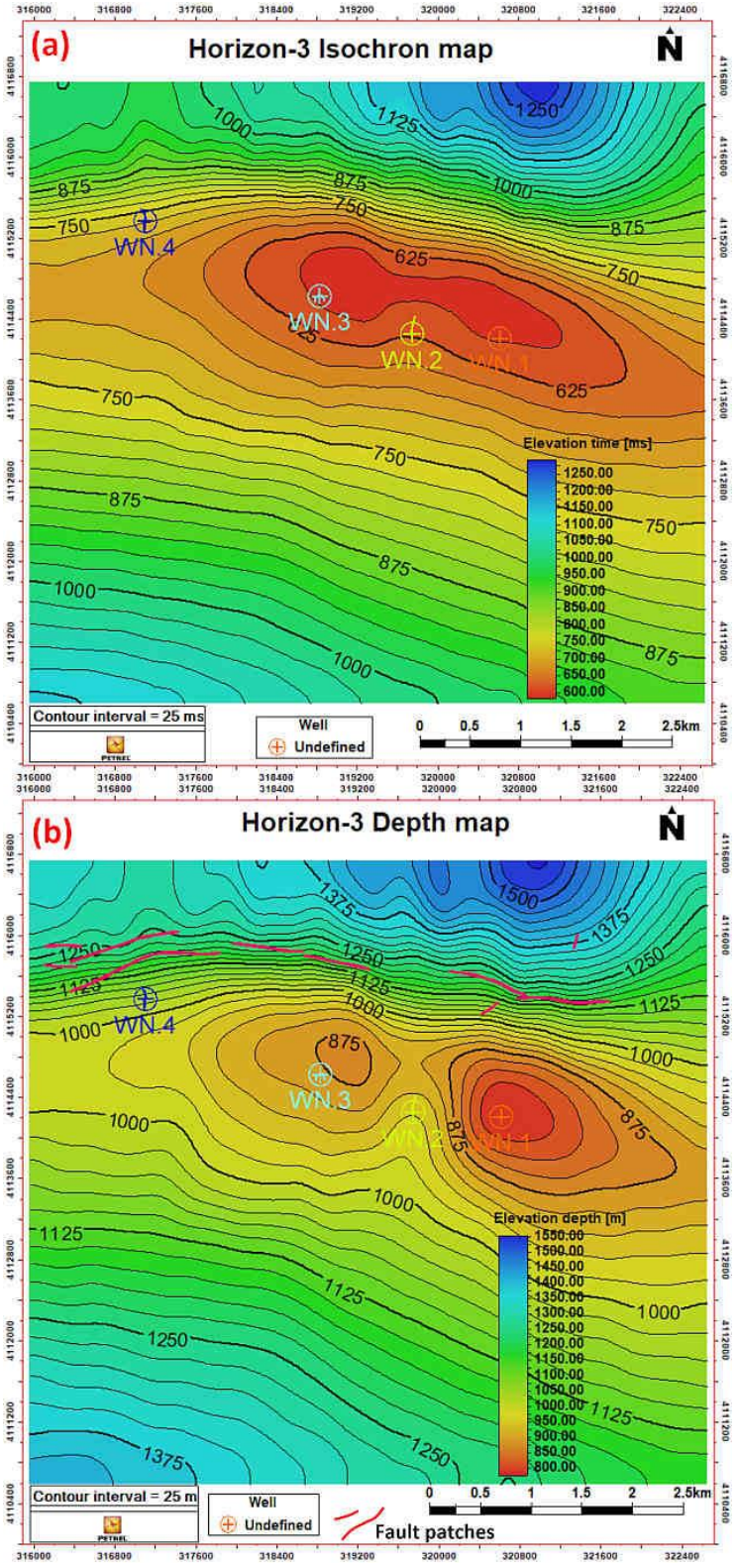

Fig.7. (a) The isochron of the Horizon-3, and (b) The depth map of the Horizon-3

The depth maps are constructed using velocities extracted from the velocity model multiplied by their isochrone surface grids. It is necessary to take into account that while using the equation (Eq.1), the computed depths from the seismic and well data should

completely match together at the wells (Al-Shuhail et al., 2017). Indeed, a perfect match between the produced depth maps of the horizons and well depths at the wells is obtained which is clearly shown in the 3D rendering (Fig. 8) and (Fig. 9). The depth maps for all the horizons seem to be similar to their corresponding isochron maps that depict the same structural features.

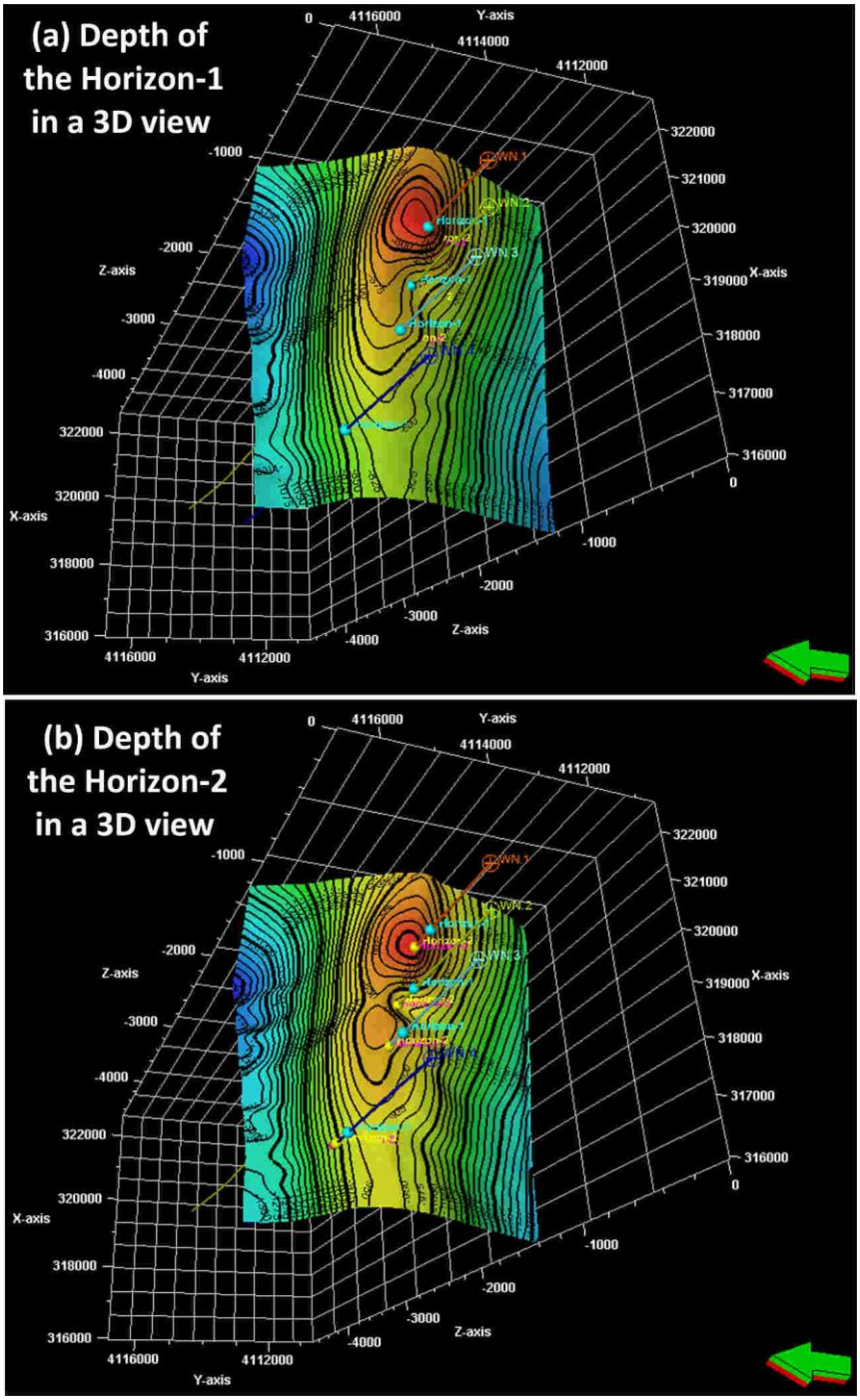

Fig.8. (a) 3D visualization of the depth of the horizon-1 with its depth at the wells, and (b) 3D visualization of the depth of the horizon-2 with its depth at the wells (arrow points northward).

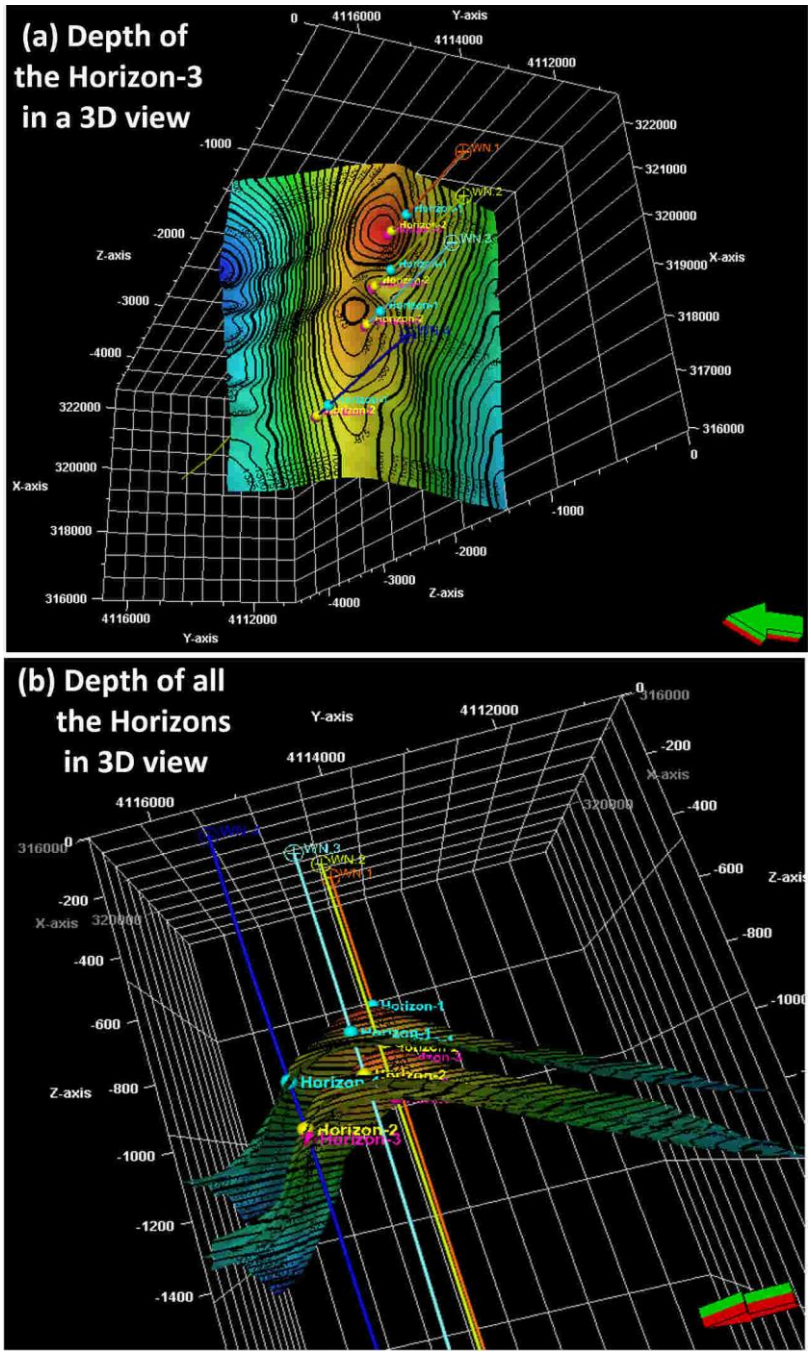

Fig.9. (a) 3D visualization of the depth of the horizon-3 with its depth at the wells, and (b) 3D visualization of the depth of all horizons with their depth at the wells (arrow points northward).

All the isochronous and depth maps display an asymmetrical doubly plunging anticlinal closure trending in East-West direction (clearly depicts Taurus style), with steeply dipping beds on the northern limb and gentle strata on the southern limb. The crest of this structure is in the eastern part at approximately 559 m, 732 m, and 744 m and extends to the1310 m, 1529.5, and 1554.7 m at the flanks at the level of the depth of the top of each of H-1, H-2, and H-3 respectively. The approximate length and width of the anticline structure are 6.4 km and 3.5 km respectively. At the top of the reservoir horizon (H-2), two domes are overlined by one anticlinal closure of the top of the cap rock horizon (H-1) which is looked upon as a structure of interest for hydrocarbon exploration. Isopach map represents a true sedimentary thickness between horizons (Osaki, 2015) rather than the horizon depth that is perpendicular to the bedding plane. The isopach map of the cap rock (Fig. 10.a) shows gradual thickening from the south and southwest towards the north and northeast, from 110m to 239m. The targeted

reservoir isopach map (Fig. 10.b) shows irregular variation in thickness throughout the study area, from less than 5m in the southern part to 82 m in the northeastern part.

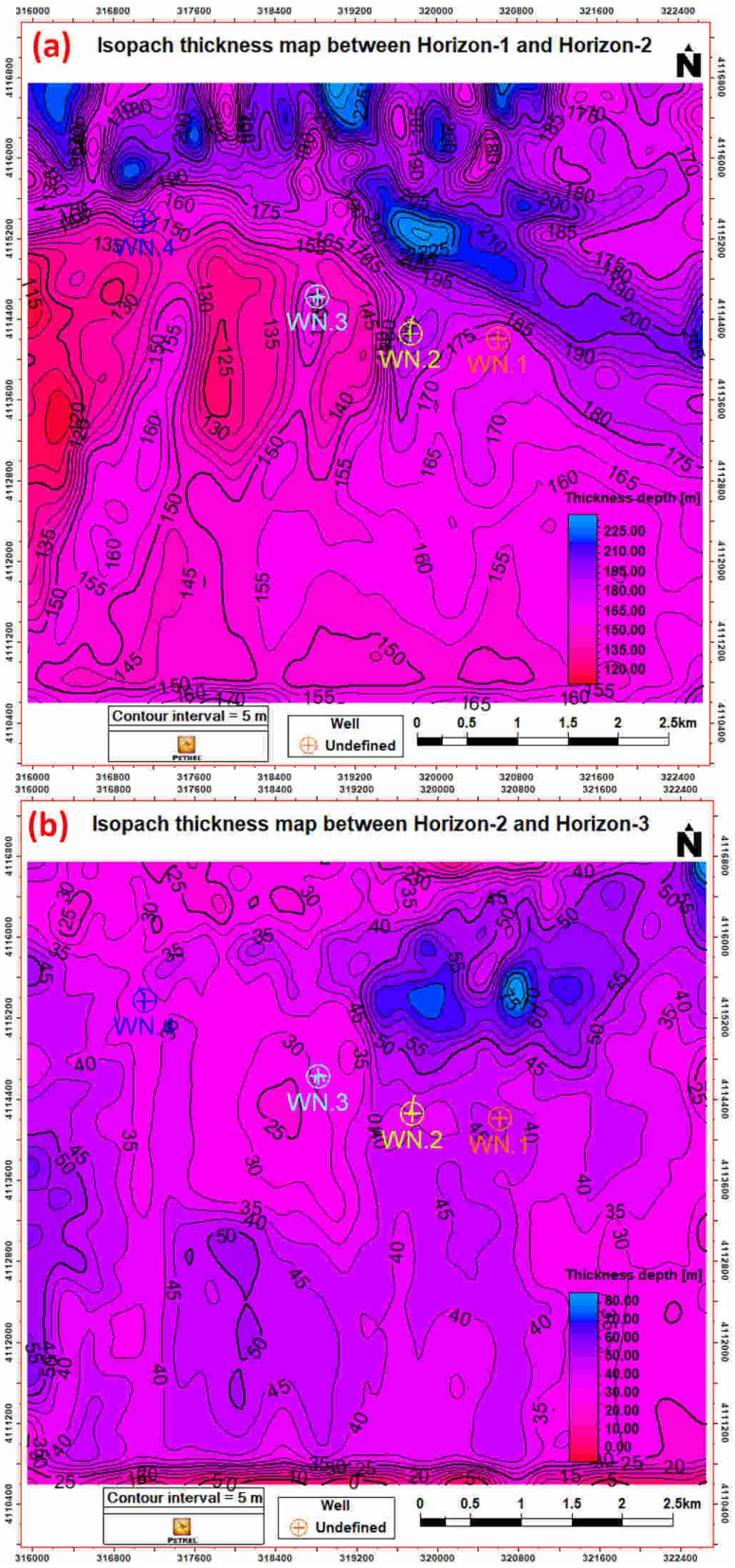

Fig.10. (a) Isopach thickness map between Horizon-1 and Horizon-2 that is regarded as the cap rock for the targeted reservoir, and (b) Isopach thickness map between Horizon-2 (the reservoir) and Horizon-3

Although perfect pillar gridding for fault modelling in the faulted area is obtained without cell distortion, it can be seen (Fig. 11.a) that there is no coincide with the horizon surfaces everywhere due to the influence of uneven topography that all the horizons have undergone folding. Thus, it is perceived that such a grid model is not suitable for use to build actual property modelling. Creating a new 3D grid for horizon modelling and then bringing all the faults from the previous fault model is a possible way to tackle this situation (Fig. 11.b).

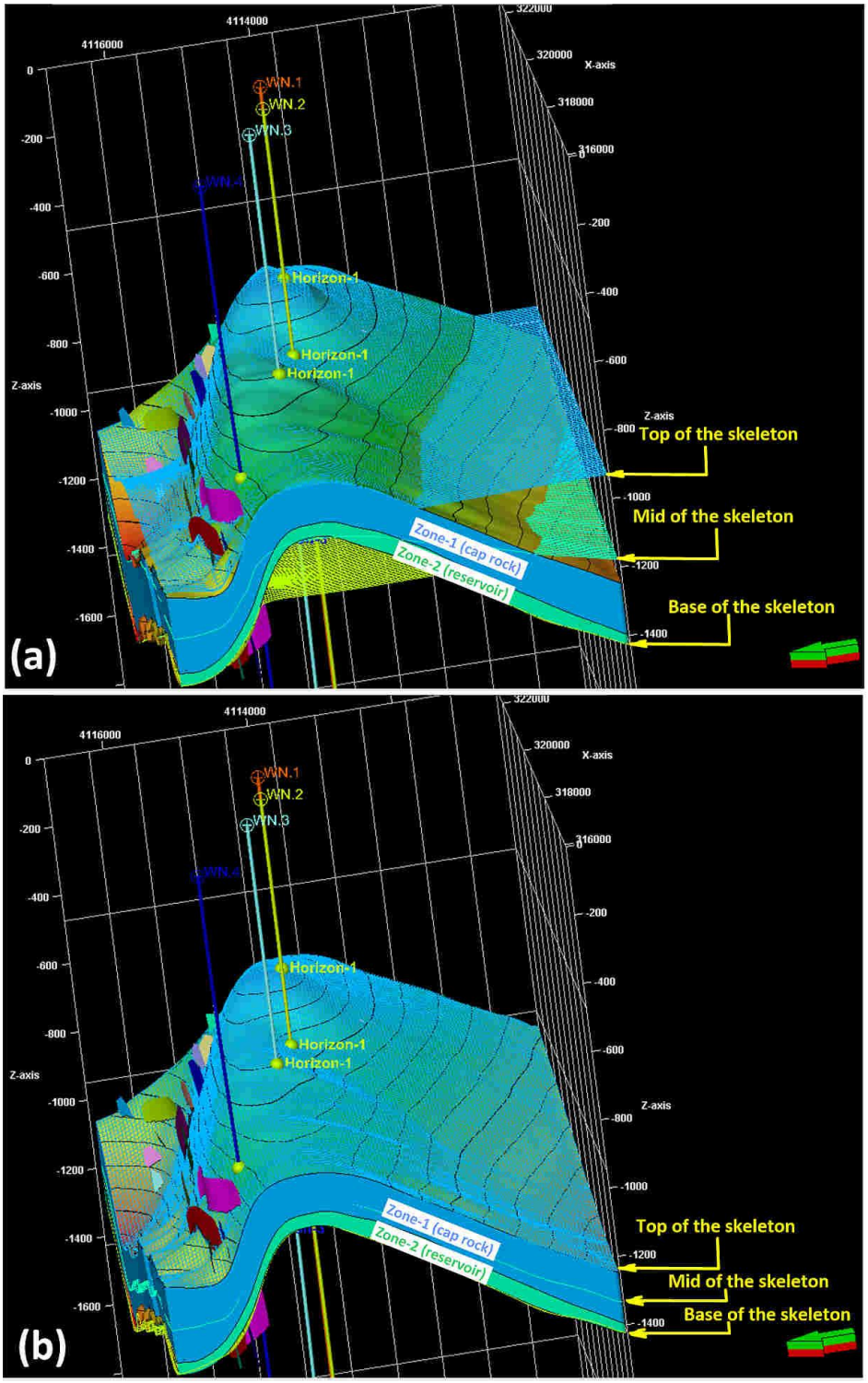

Fig.11. The grid skeleton (a) Fault-based modelling, the top of the skeleton and contours depth map of the Horizon-1 with the fault patch surfaces, and (b) Horizon-based modelling, the top of the skeleton and contours depth map of the Horizon-1 with the fault patch surfaces in their positions (arrows point northward).

Seismic conditioning is performed by applying frequency filtering (Fig. 12.b), AGC filtering (Fig. 12.c), structural smoothing (Fig. 12.d), and then picking faults and horizons on the section manually (Fig. 12.e).

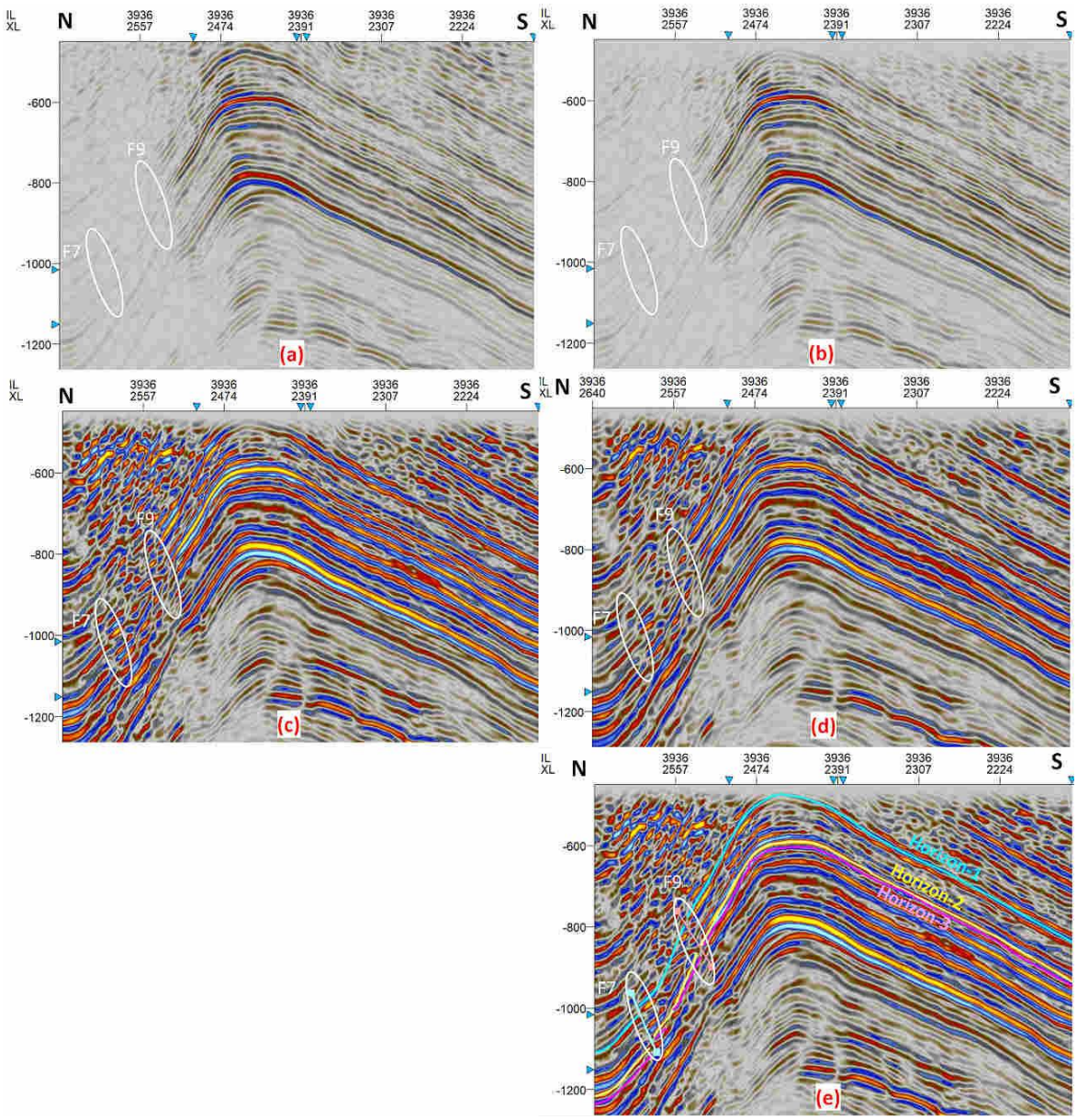

Fig.12. The seismic section of inline No. 3936 and Faults no. 7 and 9 (a) before any filtering, (b) after applying the frequency filter, (c) after implementing the AGC filter, (d) after employing structural smoothing, and (e) shows picked faults and horizons on the seismic section after running the AGC.

Eighteen picked faults in such a way are put in a 3D grid framework as shown in (Fig. 13). Next, run each of the Variance (Fig. 14.a) and Chaos (Fig. 14.b) attributes separately. Subsequently, the outputs of the last two attributes are used as inputs to the application of the ant track attribute (Fig. 14.c & d). Finally, an automatic fault extraction algorithm is applied to the Ant Tracking cube and the results were displayed in (Fig. 15) and (Fig. 16). All faults of the reverse type are small with throws ranging from 6 m to 12 m. Faults no.1, 2, 3, 4, 5, 6, and 8 cut only horizon (H1), while faults no. 7, 9, 10, 11, 12, 13, 14, 15, 16, 17, and 18 cut all the three horizons. The majority of faults almost trend in the East-West direction and few of them have an ENE-WSW orientation.

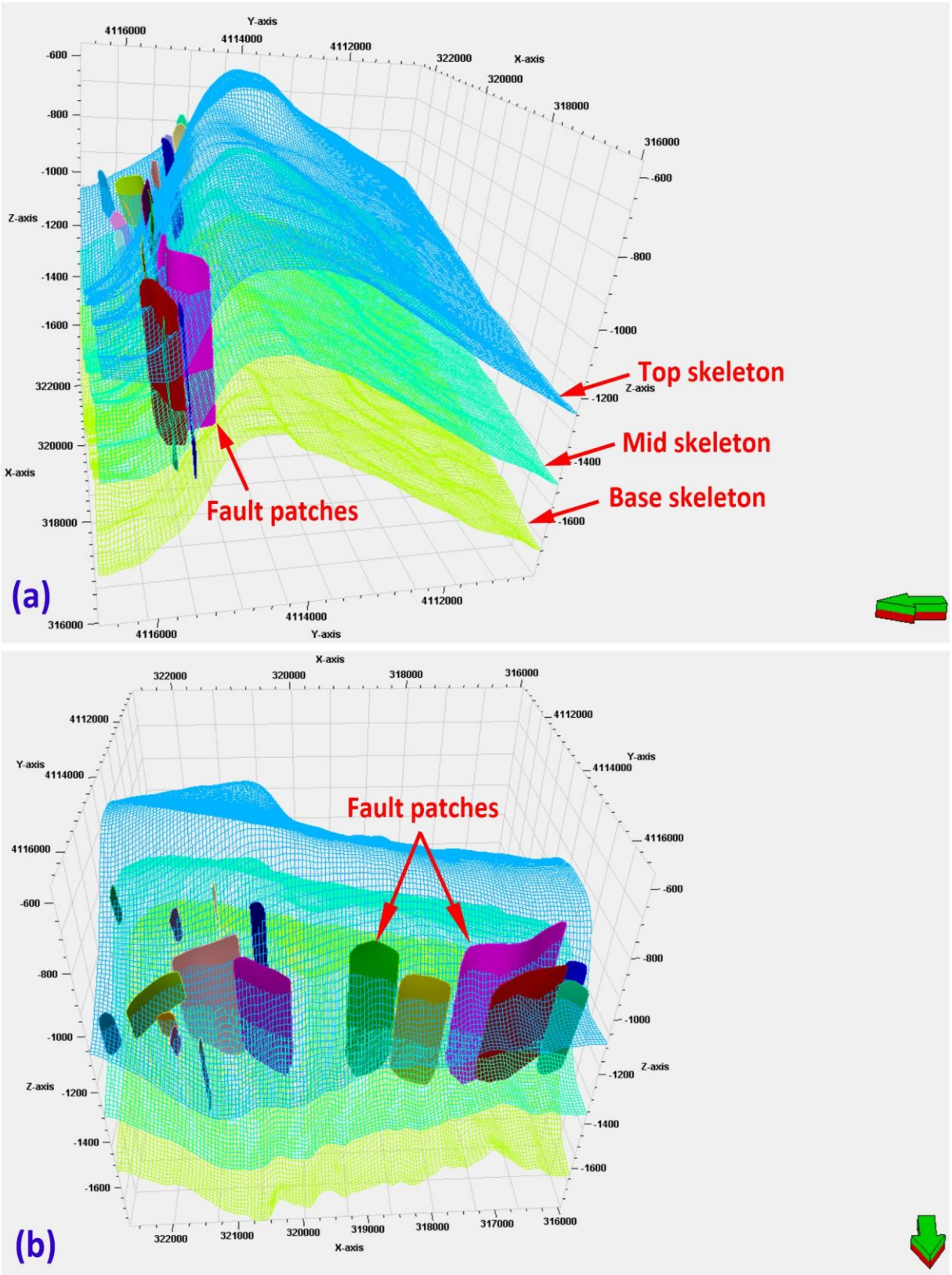

Fig.13. A 3D grid skeleton with minor fault surfaces picked on the horizons manually. (a) 3D side view (arrow points northward), (b) 3D front view (arrow points northward).

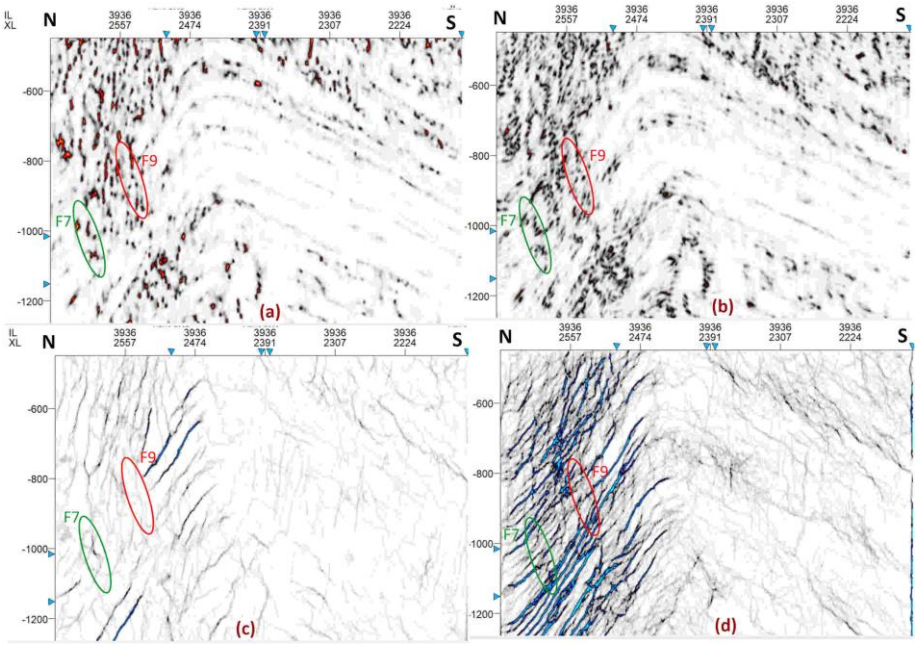

Fig.14. Inline no. 3936 and the results of different attributes (a) illustrates applying the Variance, (b) presents employing the Chaos, (c) displays the Ant Tracking of the Variance cube, and (d) shows the Ant Tracking of the Chaos cube.

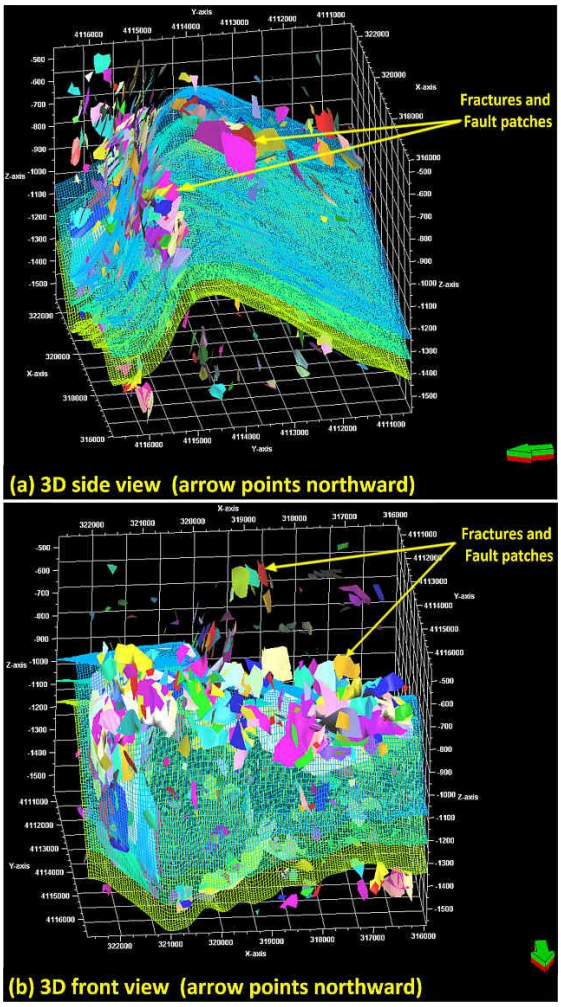

Fig.15. A 3D grid skeleton with fractures and fault patches (minor and major discontinuities) extracted automatically from a Variance-based Ant Tracking cube.

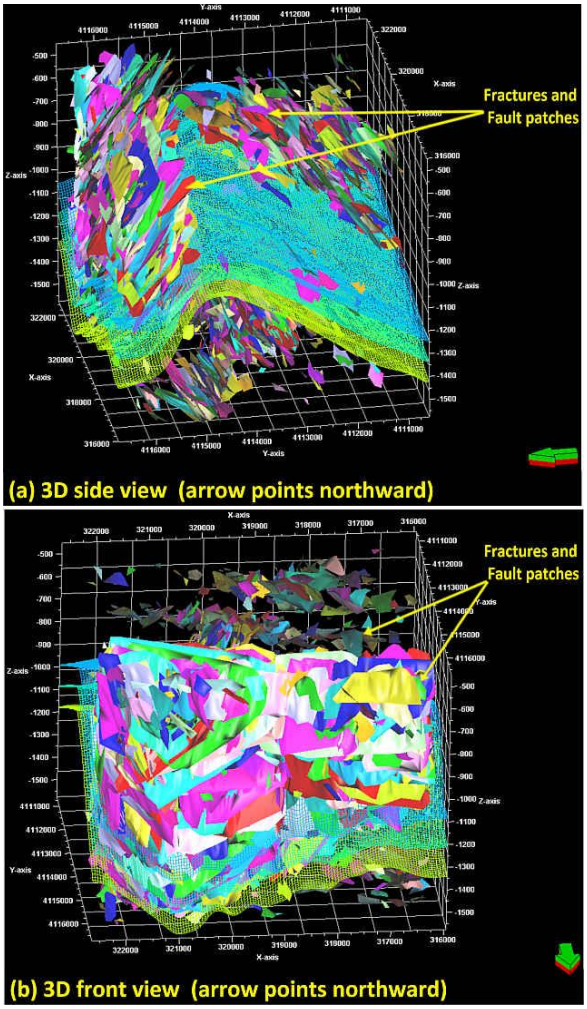

Fig.16. A 3D grid skeleton with fractures and fault patches (minor and major discontinuities) extracted automatically from a Chaos-based Ant Tracking cube.

The well-log analysis is one of the substantial means that helps to better understand reservoir characterization (Cannon, 2016). A computer-processed interpretation (CPI) analysis for reservoir formation (Horizon-2) and Horizon-3 of composite logs data from wells WN.2 and WN.3 are shown in (Fig.17.a & b). Tracks represent depths of horizons, gamma ray (GR), calliper, clay volume (VCL), water saturation (SW), permeability (Timur KT; Morris Biggs oil KMBo; Schlumberger (KSchl), total porosity (PHIT), secondary porosity (PHISEC), effective porosity, Limestone volume (Vlime), Dolomite volume (VDol), and sand volume (VSand). The permeability (KT) curve estimated by Timur formulae coincides with the (KSchl) curve estimated by the Schlumberger technique, while the (KMBo) curve by the Morris Biggs oil method with both. The KSchl permeability has been used for 3D modelling. The magnitude of porosities, VCL, and SW are represented as a percentage or a decimal fraction, whilst the permeability is expressed in millidarcy (mD) or 1/1000 of a Darcy.

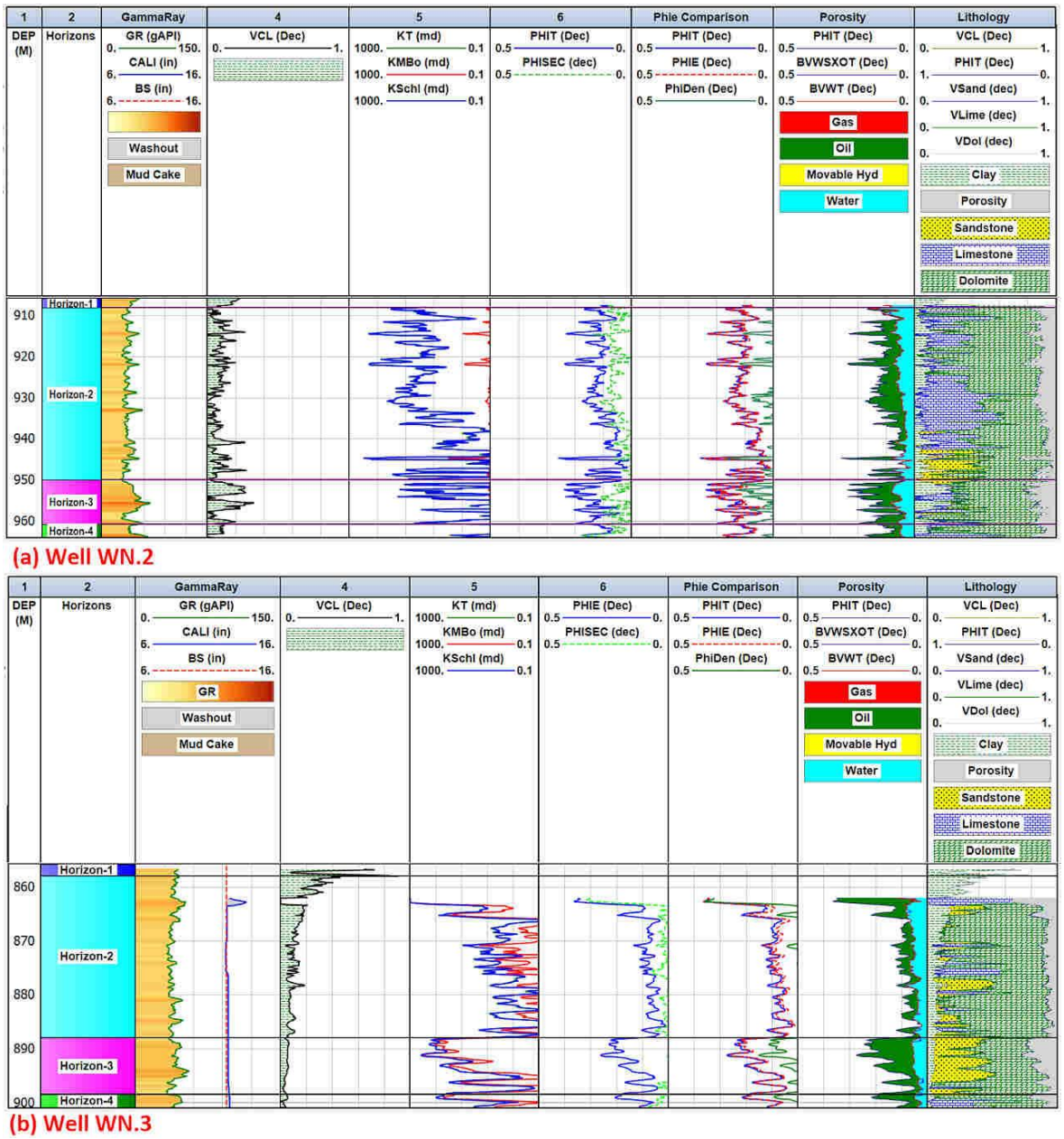

Fig.17. Computer-processed interpretation (CPI) for (a) Well WN.2, (b) Well WN.3 showing depth, horizon names, gamma ray-calliper-bit size (BS), the volume of clay, permeability, effective and secondary porosity, porosity comparison, total porosity and lithology in tracks 1,2,3, 4, 5, 6,7,8, and 9, respectively.

The combination between the neutron-density cross plot and M-N cross plot is used for determining the lithology of the target reservoir (Horizon-2) in the wells WN.2 and WN.3 (Fig. 18 and Fig.19). According to these plots, the rock formation of the reservoir is composed of dolomite, lime dolomite, and anhydritic limey dolomite.

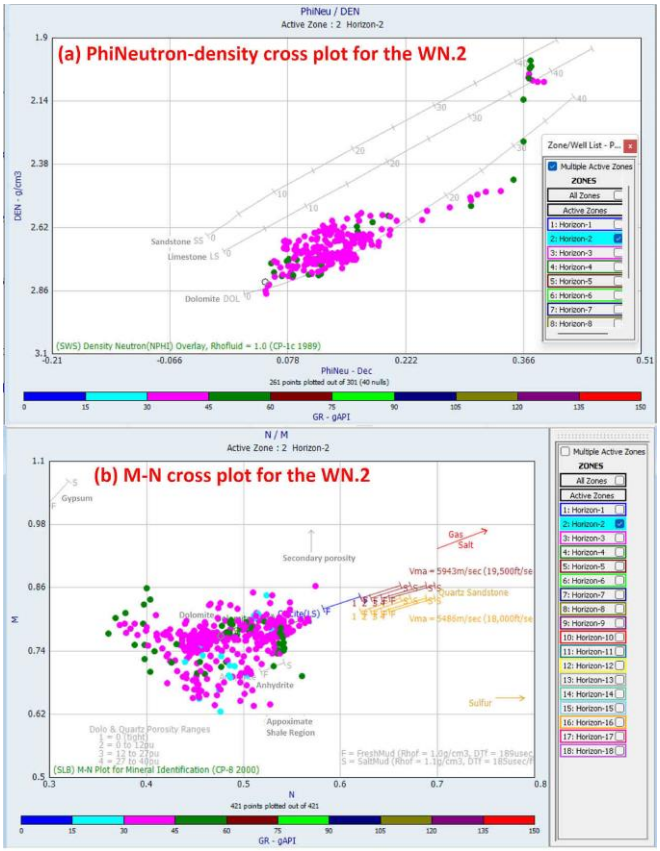

Fig.18. (a) The neutron-density cross plot, and (b) The M-N cross plot for the targeted reservoir (Horizon-2) in well WN.2.

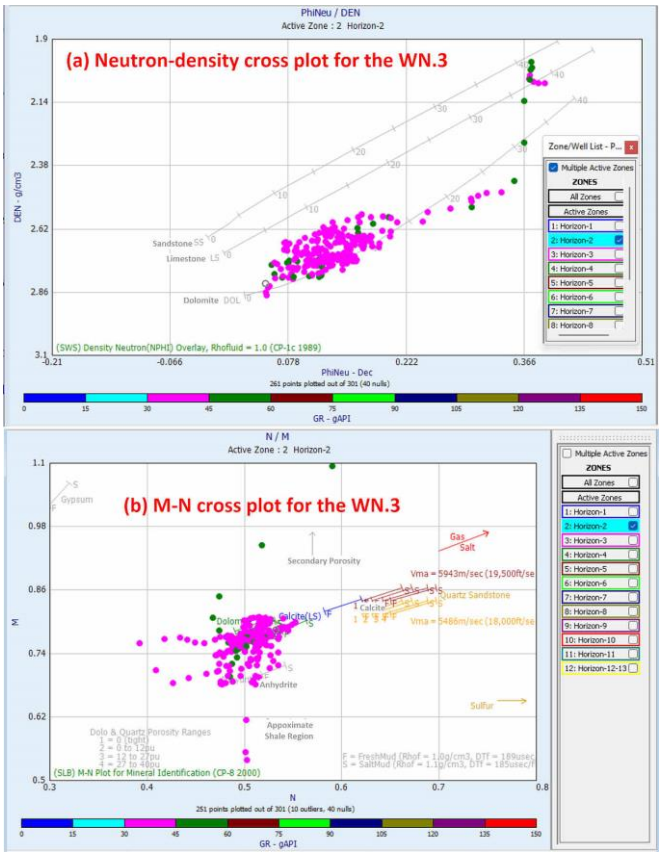

Fig.19. (a) The neutron-density cross plot, and (b) The M-N cross plot for the targeted reservoir (Horizon-2) in well WN.3.

A Buckles plot is a graph of water saturation (Sw) versus porosity including a set of diagonal curves consisting of points of equal Bulk Volume Water (BVW) (porosity multiplied by water saturation) that can be used for permeability prediction and determine lithology type of the reservoir. The estimated permeability using this approach (Fig. 20) approximately ranges from 0.01 crossed over to 1000 mD.

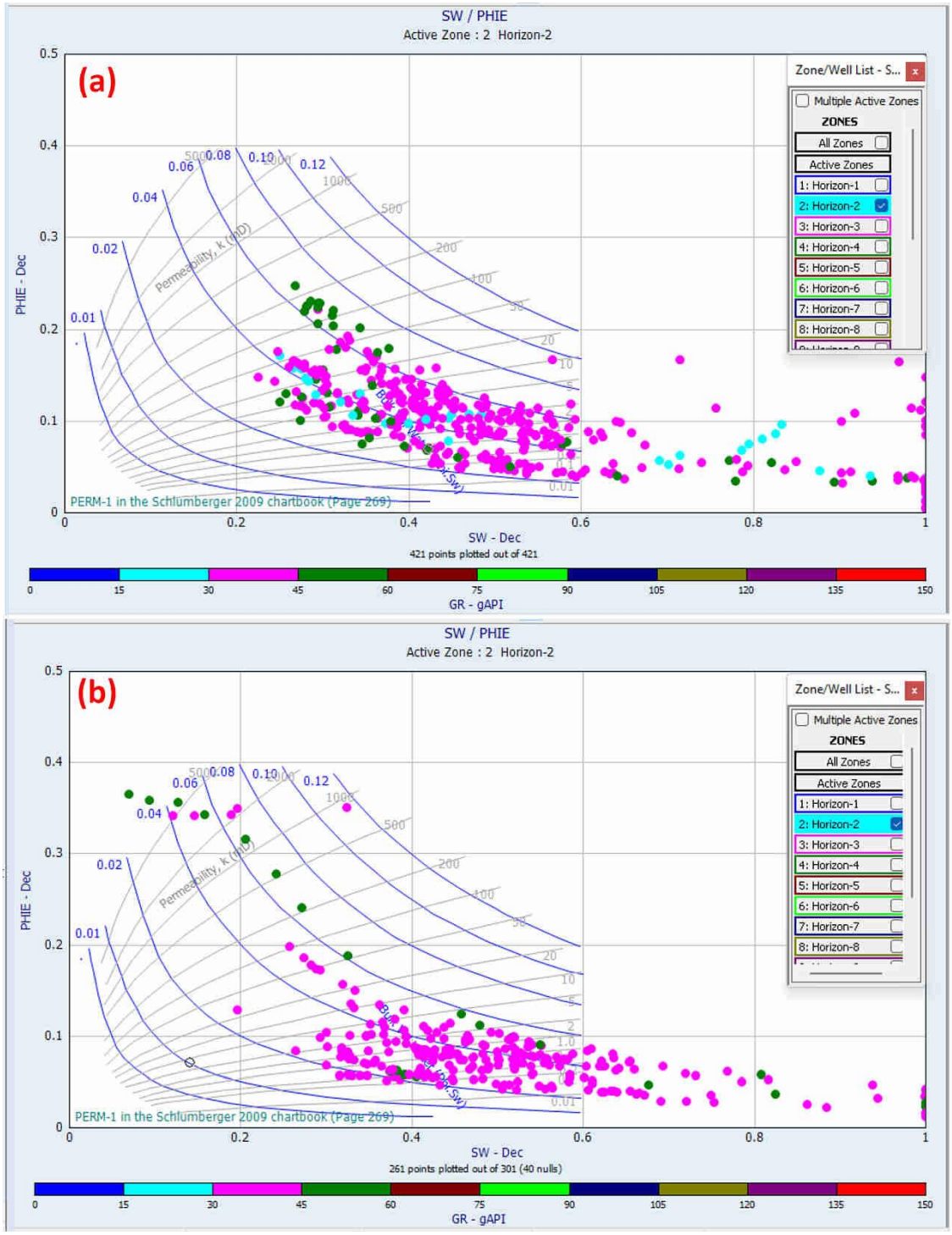

Fig.20. The figure represents the Buckles plot for the targeted reservoir (Horizon-2) in (a) Well WN.2, and (b) Well WN.3.

The porosity is the ratio of the pore volume to the total bulk volume of that rock (AL-Tool, et al., 2019). Effective Porosity is the degree of interconnected pore volume that controls the transmission of fluids (Ma et al., 2020). The effective porosity model of the

reservoir (Fig. 21) displays porosity ranging from 2.02% to 35.23%, with an average of 9.98%.

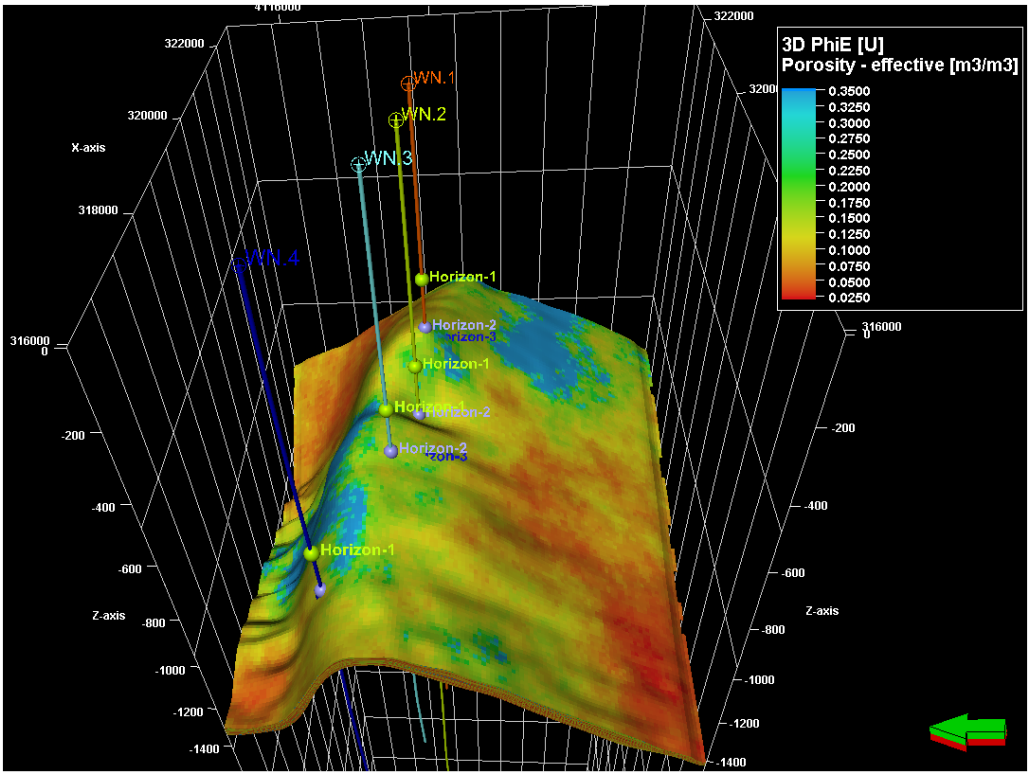

Fig.21. The 3D effective porosity model of the reservoir and wells.

Secondary porosity is formed after deposition as a result of the impact of the post-depositional fracturing and the interaction of water formation (Ali et al., 2010). The secondary porosity in carbonate rocks is considerably more significant than the primary porosity (Tiab and Donaldson, 2015), and values of the secondary porosity model (Fig. 22) lie between 0.00% to 30.34% and an average of 4.39%. According to Glover (2000), the permeability values for the rocks can vary considerably, from 1 nano-darcy, nD ($1*10^{-9}$ D) to 1 microdarcy, mD ($1*10^{-6}$ D). The permeability of reservoir rocks may generally range from 0.1 to 1000 mD or more (Tiab and Donaldson, 2015). The permeability (KSchl) model shown in (Fig. 23) displays a wide range of permeability values ranging from 0.00 mD to 1000 mD, with an average of 14.1mD. According to permeability reservoir classification by Tiab and Donaldson (2015) this reservoir is a moderate quality (Table 2).

Table 2. Classification of the reservoir qualities based on permeability according to Tiab and Donaldson (2015).

Permeability (K) in milliDarcy (mD)	Reservoir quality
k < 1mD	Poor
1mD < k < 10 mD	Fair
10 mD < k < 50 mD	Moderate
50 mD < k < 250 mD	Good
k > 250 mD	Very good

The pinkish patches roughly represent minimum permeability or impermeable area, while a tiny red patch represents maximum permeability in the southwestern part. The permeability almost has a great relationship with effective porosity, thus the low effective porosity resulted in low permeability of the reservoir. Water saturation (Sw) is the proportion of water volume present in the pores of a rock formation (Kennedy, 2015). It shows the

existence of water-saturated zones and aids in estimating the hydrocarbon saturation of the reservoir. Figure 24 displays a 3D perspective view of the water saturation model of the reservoir. The water saturation ranges between 12.53 and 100% with an average of 47.8%.

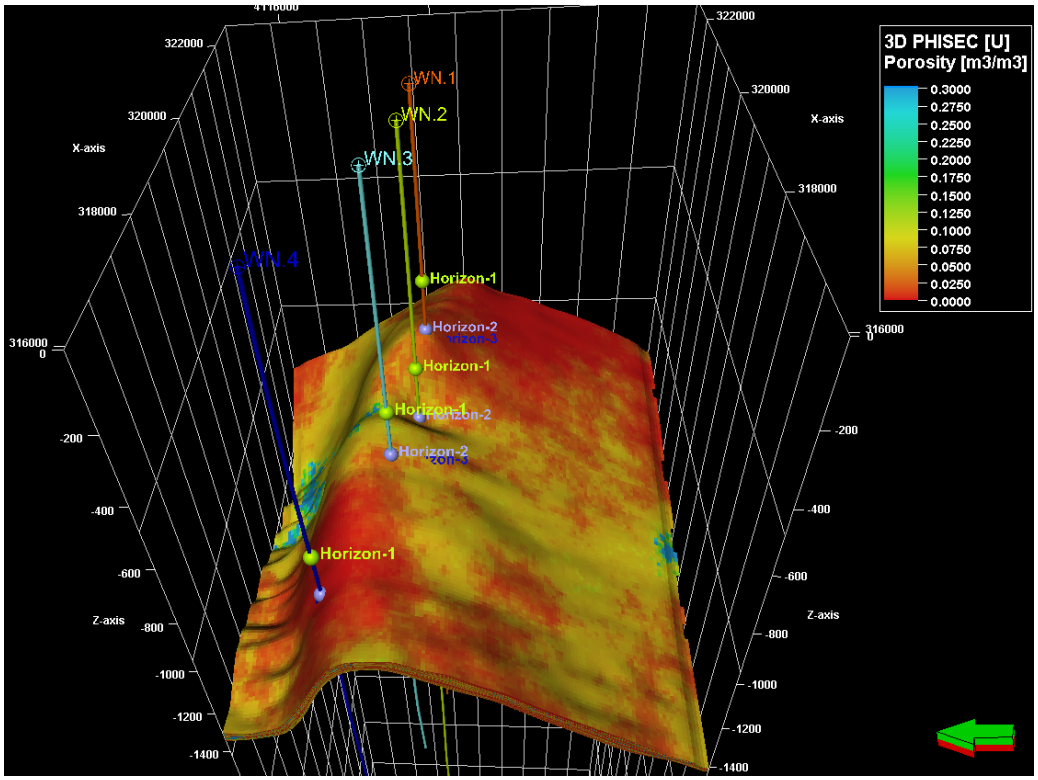

Fig.22. The 3D secondary porosity model of the reservoir and wells.

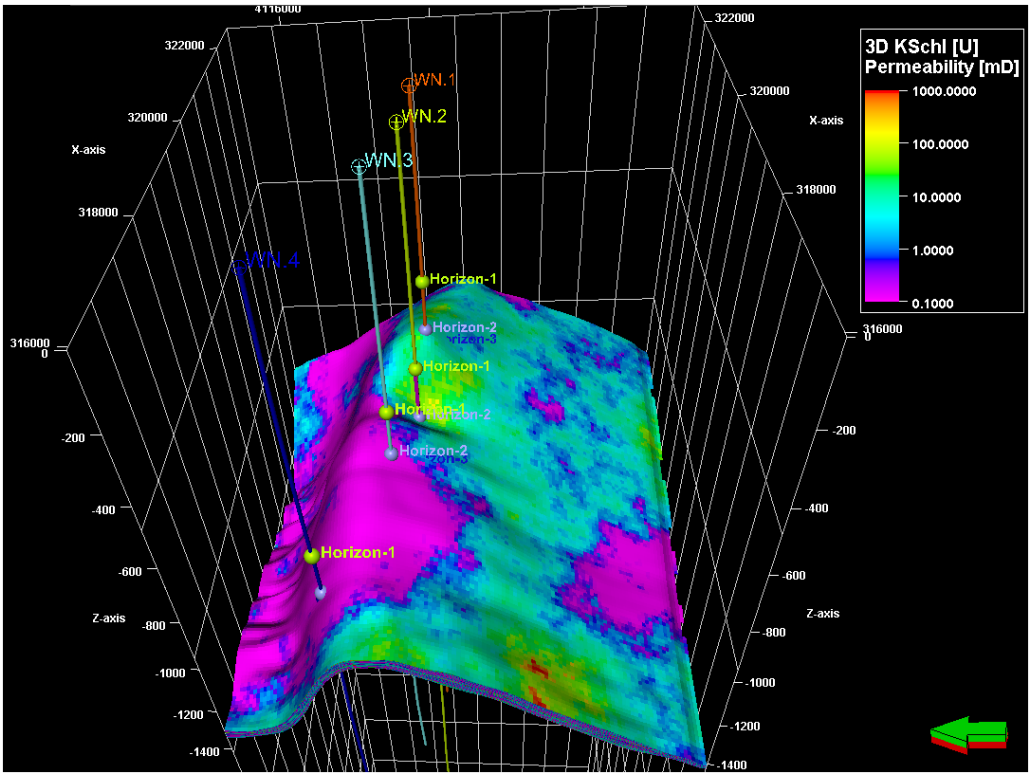

Fig.23. The 3D permeability (KSchl) model of the reservoir and wells.

The hydrocarbon saturation is estimated by using the equation:

$Sh = 100 - Sw\%$ (Asquith and Gibson, 1982)

where, Sh=hydrocarbon saturation; Sw= water Saturation. So, the mean value of the hydrocarbon saturation for the reservoirs is 52.2%.

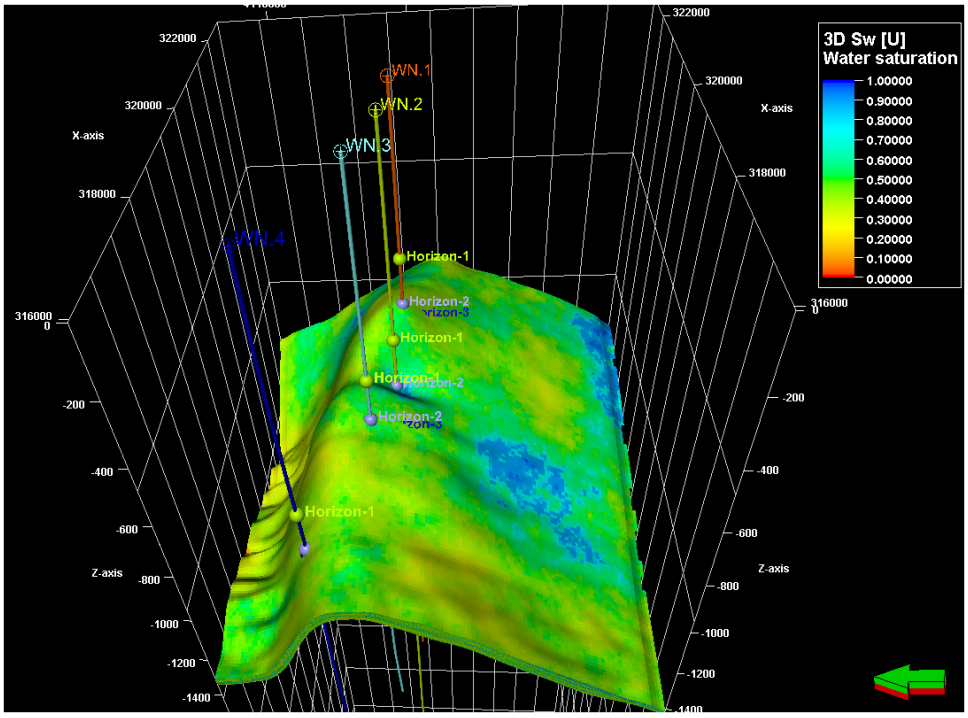

Fig.24 The 3D water saturation model of the reservoir and wells.

The clay volume model (Fig. 25) shows that the clay volume ranges from 0.00 % to 40.63%, and has an average of 9.13%.

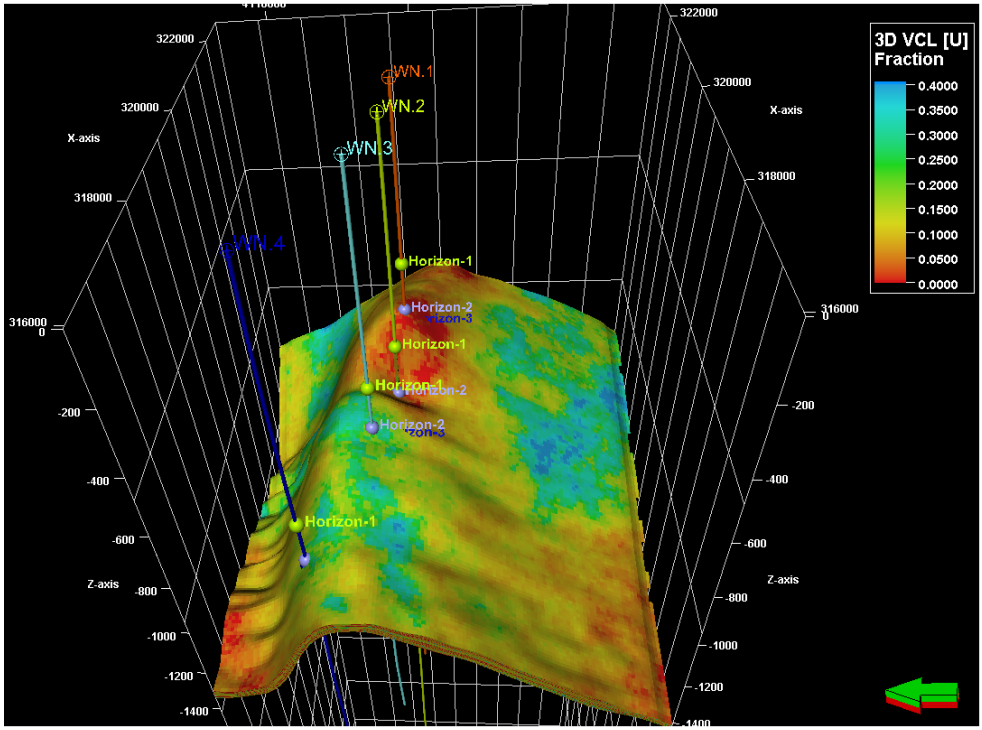

Fig.25 The 3D clay volume (VCL) model of the reservoir and wells.

Discussion

The depth maps show subsurface structural features that are almost the same pattern of structural elements that can be observed in their corresponding time maps (Fig. 5), (Fig. 6) and (Fig. 7). The asymmetrical double-plunging anticline with the E-W trend fold axis is controlled by listric faults that made it verged towards the north. It represents a rollover anticline that is bordered to the north by the main thrust fault. At the time of the closing of the Neo-Tethys Ocean and subsequent continental plate collision, tectonic compression resulted in significant thrusting and basin inversions along the northeastern Arabian plane edge (Abdulnaby et al., 2013; Sharland et al., 2001), so faulting in this structure resulted in producing several reverse secondary faults on the northern limb.

The majority of foreland folds and thrust belts reveals the presence of complicated basement relief, which is typically characterized by clear current sedimentary sequence uplift expression (Al-Kubaisi and Shakir, 2018). The East-West orientation of the anticlinal closure is consistent with the known pattern of the Taurus mountain structural style within this part of the Kurdistan Region. However, it is worth noting that an erratic to the general style can be seen in all maps that the northern limb is steeper than the southern limb. According to (Ameen, 1991) this discord can be interpreted as related to the existence of deep-seated faults that typically have no surface indication.

The collision between the Arabian plate with the Iranian and Anatolian plates started after the final closing of the Neo-Tethys Ocean in the Miocene (Abdulnaby et al., 2013). The uplifting, folding, thrusting, and dominant deformation events of the Zagros fold-thrust belt associated with this collision (Csontos et al., 2012). The belt experienced compressions due to the collision resulting in a reversal of movement on the previously formed normal faults and turning them into up thrusts (Abdulnaby et al., 2013). However, the faults have a tiny throw and do not have a great impact on the contouring of the horizons, it is preferred to mark their locations on the depth map with red sticks as displayed in (Fig. 5.b), (Fig. 6.b), and (Fig. 7.b).

The Variance (Fig. 14.a) and Chaos (Fig. 14.b) attributes successfully helped in fault and fracture capture. The Ant Tracking attribute puts out non-discontinuity events and enhances the edge structures like faults and fractures that also can aid in manual fault interpretation (Fig. 14.c & d). The produced Ant Track cubes from each of the Variance and Chaos attributes served as input for automatic fault extraction. Plenty of subtle faults and fractures are extracted from the Ant track cubes, almost trending in east-west directions (Fig. 15) and (Fig. 16).

The 3D model of the effective porosity allows for the prediction of future production and injection planning. The quantitative values of this model (Fig. 21) range between 2.02% and 35.23%, also the secondary porosity model (Fig. 22) ranges from 0.00% to 30.34%, revealing that the lithology of these carbonate rocks are not homogeneous throughout the reservoir. Buckles plot is often utilized for analyzing various reservoir parameter values (Riazi, 2022), and (Singh, 2019) selected the Buckles model to estimate and show permeability. The permeability model (Fig. 23) demonstrates a broad range from 0.00 mD to 1000 mD, and the presence of a few permeability values over 1000 mD are depicted in the Buckles model in the Well WN.3 (Fig. 20.b) also suggests an intricate nature of the pore structure of this reservoir carbonate rocks.

The water saturation shown in Fig. (23) shows values ranging from 12.53 to 100%, with an average of 47.8%, and the hydrocarbon saturation (Sh) values range from 0% to 87.47%, with an average of 52.2%. These results suggest that the wells drilled in the area (the crest of the structure) relatively have an intermediate to high water saturation and low to moderate hydrocarbon saturation. The clay volume model in Fig. (25) displays low clay content

between 0.00 % and 40.63%, with a mean of 9.13%. This low average of the clay (shale) content, which is less than 10%, suggests that the reservoir is a clean formation (AL-Tool, et al., 2019), and dolomite to lime dolomite rocks are the predominant lithology.

Relatively moderate effective porosity (Fig. 21) in blue-green colour, a relative intermediate permeability (Fig. 23) in yellow-green colour, relatively low water saturation (Fig. 24) in yellowish green colour, and low clay volume (Fig. 25) in orange colour, especially in some parts of the crest zone of anticline closure suggests that this field has a moderate prospect for hydrocarbon exploration and production.

Conclusions

The study has shown the effectiveness and versatility of integrating and using 3D seismic data, check shots, and well logs with attribute analysis in mapping subsurface features, estimation of petrophysical properties, characterization, and building a 3D static model for the targeted reservoir. The main conclusions are as follows:

- The isochronous and depth maps show a doubly plunging anticlinal closure trending in the East-West direction (Taurus style) with an area of 6.4 km length and 4.5 km width. Its northern limb is steeper than the southern limb, which is inconsistent with the general structural style in this region. This abnormal situation may be due to the local tectonic activity generating stress toward the north direction.
- The northern part of the anticlinal closure (rollover anticline) is dissected by eighteen minor reversal faults with a tiny throw range between 6m and 12m oriented in E-W and ENE-WSW direction. After manually detecting and interpreting the faults, they were used for building 3D static modelling.
- The top, mid, and bottom of the produced skeletal framework by pillar gridding process from the fault modelling has shown inconsistency with the top of horizons everywhere outward from the faulted area, building a new 3D grid by horizon modelling and then incorporating the faults into it can be one way for amending the grid.
- The attribute analysis enhanced and improved fault interpretation in the 3D seismic data set, and showed their effective role in automatic fault and fracture extraction.
- The analysis performed on the reservoir zone, cross-plots show good capabilities to determine and delineate porosity and lithology in well logs data.
- The cross-plots show that the reservoir consists mainly of dolomite, lime dolomite, and anhydritic limey dolomite.
- The 3D models of petrophysical parameters reveal that the reservoir has moderate-quality reservoirs.

Acknowledgments

Sincere thanks to the Ministry of Natural Resources (MNR) of the Kurdistan Region Government (KRG) and oil companies operating in the region for providing necessary 3D seismic data and well logs. Grateful appreciation goes to each of Schlumberger and Senergy companies for making free licenses of their valuable software (Petrel Suite seismic interpretation and Interactive Petrophysics IP) for academic research.

Conflict of Interest

The authors declare that there is no conflict of interest

References

Abdula, R.A., 2017. Geothermal gradients in Iraqi Kurdistan deduced from bottom hole temperatures. Egypt. J. Pet. 26, 601–608. https://doi.org/10.1016/j.ejpe.2016.08.007

Abdulnaby, W., Mahdi, H., Numan, N.M.S., Al-Shukri, H., 2013. Seismotectonics of the Bitlis-Zagros Fold and Thrust Belt in Northern Iraq and Surrounding Regions from Moment Tensor Analysis. Pure Appl. Geophys. 171, 1237–1250. https://doi.org/10.1007/s00024-013-0688-4

Al-Azzawi, N.K., 2013. Paleo and Neo-Tectonics of the Mosul Fault and its Impact on the Tectonics of the Foreland Area of Iraq. Iraqi Natl. J. Earth Sci. 13, 59–74.

Ali, S.A., Clark, W.J., Moore, W.R., Dribus, J.R., 2010. Diagenesis and reservoir quality. Oilf. Rev. 22, 14–27.

Aliouane, L., Ouadfeul, S.A., 2014. Sweet spots discrimination in shale gas reservoirs using seismic and well-logs data. A case study from the Worth basin in the Barnett shale. Energy Procedia 59, 22–27. https://doi.org/10.1016/j.egypro.2014.10.344

Al-Kubaisi, M.S., Shakir, M.M., 2018. Structural analysis for the plunge areas of bekhair, brifca, dohuk and zawita anticlines Northern Iraq using seismic sections. Iraqi Geol. J. 51, 56–68.

Al-Ridha, N.A., AL-Sharaa, G.H. and Muhsin, S.U., 2018. Structural subsurface model of Samawa-Diwan area (south of Iraq). Iraqi Journal of Science, pp.1920-1935. h

Alsadi, H.N., 2017. Seismic hydrocarbon exploration: 2d and 3d techniques, Advances in Oil and Gas Exploration and Production. Springer International Publishing Switzerland. https://doi.org/10.1007/978-3-319-40436-3

Al-Shuhail, A.A., Al-Dossary, S.A., Mousa, W.A., 2017. Seismic data interpretation using digital image processing. John Wiley & Sons.

AL-Tool, Z. M.H., Almallah, I.A., Al-Najm, F.M., 2019. Petrophysical properties evaluation using well logging of the upper sand member of Zubair Formation in Zubair oil Field, Southern Iraq. Basrah J. Sci. 37, 456–480.

Ameen, M.S., 1991. Possible forced folding in the Taurus–Zagros Belt of northern Iraq. Geol. Mag. 128, 561–584. https://doi.org/10.1017/S0016756800019695

Aqrawi, A.A.M., Goff, J.C., Horbury, A.D., Sadooni, F.N., 2010. The petroleum geology of Iraq. Scientific press.

Arifin, M.T., 2016. Reservoir characterization using seismic attributes and inversion analysis of Globigerina Limestone reservoir, Madura Strait, Indonesia. Bull. Earth Sci. Thail. 8, 179–189. https://doi.org/10.29118/IPA.50.17.267.G

Ashraf, U., Zhu, P., Yasin, Q., Anees, A., Imraz, M., Mangi, H.N., Shakeel, S., 2019. Classification of reservoir facies using well log and 3D seismic attributes for prospect evaluation and field development: A case study of Sawan gas field, Pakistan. J. Pet. Sci. Eng. 175, 338–351. https://doi.org/10.1016/j.petrol.2018.12.060

Asquith, G.B., Gibson, C.R., 1982. Basic well log analysis for geologists. American Association of Petroleum Geologists Tulsa. https://doi.org/10.1306/Mth3425

Bueno, J.F., Honório, B.C.Z., Kuroda, M.C., Vidal, A.C., Pereira Leite, E., 2014. Structural and stratigraphic feature delineation and facies distribution using seismic attributes and well log analysis applied to a Brazilian carbonate field. Interpretation 2, SA83–SA92. https://doi.org/10.1190/INT-2013-0087.1

Cannon, S., 2016. Petrophysics a practical guide, WD info. John Wiley & Sons, Ltd.

Csontos, L., Sasvári, Á., Pocsai, T., Kósa, L., Salae, A.T., Ali, A., 2012. Structural evolution of the northwestern Zagros, Kurdistan Region, Iraq: Implications on oil migration. GeoArabia 17, 81–116. https://doi.org/10.2113/geoarabia170281

Donahoe, T., Gao, D., 2016. Application of 3D seismic attribute analysis to structure interpretation and hydrocarbon exploration southwest Pennsylvania, Central Appalachian Basin: A case study. Interpretation 4, T291–T302. https://doi.org/10.1190/INT-2015-0080.1

Doski, J.A.H., McClay, K., 2022. Tectono-stratigraphic evolution, regional structure and fracture patterns of the Zagros fold-thrust belt in the Duhok region, Kurdistan, northern Iraq. Tectonophysics 838. https://doi.org/10.1016/j.tecto.2022.229506

Edilbi, A.N.F., Kolo, K., Muhammed, N.R., Yasin, S.R., Mamaseni, W.J., Akram, R., 2019. Source rock evaluation of shale intervals of the Kurra Chine Formation, Kurdistan Region-Iraq: An organic geochemical and basin modeling approach. Egypt. J. Pet. 28, 315–321. https://doi.org/10.1016/j.ejpe.2019.06.003

English, J.M., Lunn, C.A., Ferreira, L., Yacu, G., 2015. Geologic evolution of the Iraqi Zagros, and its influence on the distribution of hydrocarbons in the Kurdistan region. Am. Assoc. Pet. Geol. Bull. 99, 231–272. https://doi.org/10.1306/06271413205

Glover, P.W.J., 2000. Petrophysics, University of Aberdeen, UK.

Grabeel, H.H., 2018. Application of Seismic Attributes for 3-D Seismic Visualization Contributed in Structural and Stratigraphic Interpretation of the Tangahoe and Farewell Formations in the Kupe Field, Taranaki Basin, New Zealand. MSc. Thesis. Missouri University of Science and Technology.

Hart, B.S., 1999. Definition of subsurface stratigraphy, structure and rock properties from 3-D seismic data. Earth Sci. Rev. 47, 189–218. https://doi.org/10.1016/S0012-8252(99)00029-X

Jassim, S.Z., Goff, J.C., 2006. Geology of Iraq. DOLIN, sro, distributed by Geological Society of London.

Jiratitipat, T., 2020. Mapping of fault system related to salt movement inVolve field, offshore Norway, North Sea. Bull. Earth Sci. Thail. 12, 25–36. https://ph01.tci-thaijo.org/index.php/bestjournal/article/view/246792

Johann, P., de Castro, D.D., Barroso, A.S., 2001. Reservoir Geophysics: Seismic Pattern Recognition Applied to Ultra-Deepwater Oilfield in Campos Basin, Offshore Brazil. SPE. https://doi.org/10.2118/69483-ms

Kennedy, M., 2015. Practical Petrophysics, Developments in Petroleum Science. Elsevier B.V.

Khawaja, A.M., Thabit, J.M., 2021. Interpretation of 3D seismic reflection data to reveal stratigraphic setting of the reservoir of mishrif formation in Dujaila Oil Field, Southeast of Iraq. Iraqi J. Sci. 62, 2250–2261. https://doi.org/10.24996/ijs.2021.62.7.14

Koshnaw, R.I., Stockli, D.F., Horton, B.K., Teixell, A., Barber, D.E., Kendall, J.J., 2020. Late Miocene Deformation Kinematics Along the NW Zagros Fold-Thrust Belt, Kurdistan Region of Iraq: Constraints From Apatite (U-Th)/He Thermochronometry and Balanced Cross Sections. Tectonics 39. https://doi.org/10.1029/2019TC005865

Kozak, S., 2018. Comparison of fracture detection methods applied on the Kerry 3D seismic, Taranaki Basin, New Zealand. M. Sc. Thesis. Montan University, Leoben.

Ma, B., Hu, Q., Yang, S., Yin, N., Qiao, H., Zhang, T., Meng, M., 2020. Multiple Approaches to Quantifying the Effective Porosity of Lacustrine Shale Oil Reservoirs in Bohai Bay Basin, East China. Geofluids 2020. https://doi.org/10.1155/2020/8856620

Ogbamikhumi, A., Aderibigbe, O.T., 2019. Velocity modelling and depth conversion uncertainty analysis of onshore reservoirs in the Niger Delta basin. J. Cameroon Acad. Sci. 14, 239. https://doi.org/10.4314/jcas.v14i3.7

Ortiz, J.M., 2020. Introduction to sequential Gaussian simulation.Predictive Geometallurgy

and Geostatistics Lab, Annual Report 2020, paper 2020-01, 7-19. Queen's University.
Osaki, L.J., 2015. 3D Seismic Attributes Analysis And Reserve Estimation Of Guramala Field'', Coastal Swamp Depobelt, Niger Delta. M. Sc Diss. Fed. Univ. Technol.
Osinowo, O.O., Ayorinde, J.O., Nwankwo, C.P., Ekeng, O.M., Taiwo, O.B., 2018. Reservoir description and characterization of Eni field Offshore Niger Delta, southern Nigeria. J. Pet. Explor. Prod. Technol. 8, 381–397. https://doi.org/10.1007/s13202-017-0402-7
Pedersen, S.I., Randen, T., Sønneland, L., Steen, Ø., 2002. Automatic fault extraction using artificial ants, in: SEG Annual Meeting.Salt Lake City, Utah. OnePetro. . https://doi.org/10.1190/1.1817297
Reif, D., Decker, K., Grasemann, B., Peresson, H., 2012. Fracture patterns in the Zagros fold-and-thrust belt, Kurdistan Region of Iraq. Tectonophysics 576–577, 46–62. https://doi.org/10.1016/j.tecto.2012.07.024
Riazi, Z., 2022. Rock Typing by Bulk Volume Water Method in the Carbonate Reservoirs 13. https://doi.org/10.35248/2157-7463.22.13.451
Schlumberger, 2010. Petrel Seismic to Simulation Software Version 2010 for Windows , help manual. Schlumberger.
Sharland, P., Archer, R., Casey, D., Davies, R., Hall, S.H., Heward, A., Horbury, A., Simmons, M., 2001. Arabian Plate Sequence Stratigraphy., GeoArabia Special Publication. Gulf PetroLink, Bahrain.
Singh, N.P., 2019. Permeability prediction from wireline logging and core data: a case study from Assam-Arakan basin. J. Pet. Explor. Prod. Technol. 9, 297–305. https://doi.org/10.1007/s13202-018-0459-y
Ten Veen, J., de Haan, H., de Bruin, G., Holleman, N., Schöler, W., 2019. Seismic interpretation and depth conversion of the Dinantian carbonates in the Dutch subsurface. SCAN Dinantian Rep.
Tiab, D., Donaldson, E.C., 2015. Petrophysics: Theory and Practice of Measuring Reservoir Rock and Fluid Transport Properties: Fourth Edition, Petrophysics: Theory and Practice of Measuring Reservoir Rock and Fluid Transport Properties: Fourth Edition. Gulf Professional Publishing is an imprint of Elsevier. https://doi.org/10.1016/C2014-0-03707-0
Toba, A., Ideozu, R.U., and Ibe, A.C., 2018. Modelling of reservoirs in Awe- Field, eastern
Niger Delta, Nigeria. J. Appl. Geol. Geophy. 6(4): 36- 46. https://doi.org/10.9790/0990-0604023646
Van Bellen, R.C., Dunnington, H. V, Wetzel, R., Morton, D.M., 1959. Lexique stratigraphique international, v. 3, Asie, fasc. 10a, Iraq (Mesozoic and Paleozoic), 333 p. Paris, Cent. Rech. Sci. Internat. Geol Cong Comm Strat.
Varela, O.J., Torres-Verdín, C., Lake, L.W., 2006. On the value of 3D seismic amplitude data to reduce uncertainty in the forecast of reservoir production. J. Pet. Sci. Eng. 50, 269–284. https://doi.org/10.1016/j.petrol.2005.11.004
Zainy, M.T., Al-Ansari, N., Bauer, T.E., Ask, M., 2017. The Tectonic and Structural Classifications of the Western Part of the Zagros Fold and Thrust Belt, North Iraq, Review and Discussion. J. Earth Sci. Geotech. Eng. 7, 1792–9660.